Cell

Nucleation and Transport Organize Microtubules in Metaphase Spindles

Jan Brugués,[1,2,*] Valeria Nuzzo,[2] Eric Mazur,[2] and Daniel J. Needleman[1,2]
[1]Department of Molecular and Cellular Biology and Center for Systems Biology, Harvard University, 52 Oxford Street, Cambridge, MA 02138, USA
[2]School of Engineering and Applied Sciences, Harvard University, 9 Oxford Street, Cambridge, MA 02138, USA
*Correspondence: jbrugues@fas.harvard.edu
DOI 10.1016/j.cell.2012.03.027

SUMMARY

Spindles are arrays of microtubules that segregate chromosomes during cell division. It has been difficult to validate models of spindle assembly due to a lack of information on the organization of microtubules in these structures. Here we present a method, based on femtosecond laser ablation, capable of measuring the detailed architecture of spindles. We used this method to study the metaphase spindle in *Xenopus laevis* egg extracts and found that microtubules are shortest near poles and become progressively longer toward the center of the spindle. These data, in combination with mathematical modeling, imaging, and biochemical perturbations, are sufficient to reject previously proposed mechanisms of spindle assembly. Our results support a model of spindle assembly in which microtubule polymerization dynamics are not spatially regulated, and the proper organization of microtubules in the spindle is determined by nonuniform microtubule nucleation and the local sorting of microtubules by transport.

INTRODUCTION

In Eukaryotes, the spindle segregates chromosomes during cell division. Spindles are composed of microtubules and associated proteins that regulate microtubule polymerization dynamics, transport, and nucleation, but the manner in which these activities generate bipolar spindles—and the extent to which they are spatially regulated—is not understood.

A wide variety of models have been proposed to explain how the spatial and temporal regulation of microtubules and associated proteins results in the assembly of the spindle (Dumont and Mitchison, 2009; Goshima and Scholey, 2010; Mogilner and Craig, 2010). Some models postulate that the organization of the spindle is controlled by reaction-diffusion systems of soluble proteins that stabilize and nucleate microtubules near chromosomes (Karsenti and Vernos, 2001; Sampath et al., 2004). Others argue that the architecture of the spindle is governed by selective stabilization (Greenan et al., 2010) or destabilization of microtubules near spindle poles (Loughlin et al., 2010). Spindle structure might also be determined by a tight regulation of the lengths of individual microtubules, even without spatial variations in microtubule stability (Howard and Hyman, 2007), a balance of forces between different mechanical elements (Dumont and Mitchison, 2009), the distance a microtubule travels before it depolymerizes (Burbank et al., 2007), or the nucleation of microtubules off of other microtubules (Goshima et al., 2008). Different mechanisms could also be present in other systems (Goshima and Scholey, 2010). These models make distinct predictions for the lengths and organization of microtubules in the spindle—for example, if microtubules are stabilized around chromosomes, they would be longer near chromosomes, whereas if microtubules are stabilized near spindle poles, they would be longer at that location. However, there is currently insufficient structural information on spindles to determine the validity of these models.

Microtubules in spindles are too dense to resolve with light microscopy, even with modern super-resolution techniques (Schermelleh et al., 2010). Individual microtubules in spindles can be clearly seen with electron microscopy (EM), but the largest spindles whose structures have been completely reconstructed to date are from the yeasts *Schizosaccharomyces pombe* (Ding et al., 1993) and *Saccharomyces cerevisiae* (Winey et al., 1995, 2005), which are approximately 2 microns long at metaphase and contain ∼40 microtubules. Spindles from Metazoans can have volumes thousands to tens of thousands of times larger than those of yeasts, so obtaining detailed EM data on these structures is challenging. Partial reconstructions of larger spindles (McIntosh and Landis, 1971; Mastronarde et al., 1993; Heald et al., 1997; Srayko et al., 2006) have revealed that these spindles can contain thousands to hundreds of thousands of microtubules, the majority of which are nonkinetochore microtubules, that do not make direct contact with chromosomes. However, the limited extent of these reconstructions is insufficient to determine the organization and lengths of microtubules in these spindles. Indirect methods have shown that microtubule plus ends and minus ends are located throughout larger spindles and have been used to argue that microtubule lengths are broadly distributed in these structures (Burbank et al., 2006; Yang et al., 2007). However these techniques are unable to resolve spatial variations in microtubule length and organization within spindles, greatly limiting the conclusions that can be drawn from them.

We have developed a method, based on femtosecond laser ablation, capable of quantitatively measuring the length

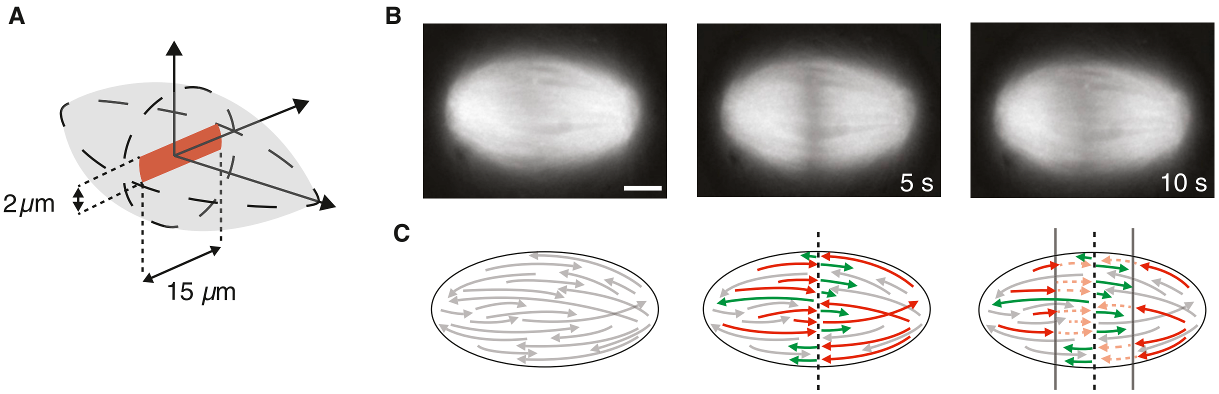

Figure 1. Laser Ablation Induces Fronts of Synchronous Microtubule Depolymerization

(A) Geometry of a laser cut in the spindle.

(B) Series of fluorescent images of a spindle taken before the cut and at 5 s and 10 s after the cut. Scale bar, 10 μm. See also Movie S1.

(C) Graphical representation of the cut microtubules from (B). The laser-cut microtubules (gray) generate a pair of microtubules with new plus ends (red) and new minus ends (green). The newly generated minus ends (green) remain stable, whereas the newly generated plus ends depolymerize (red), which creates two depolymerization fronts of opposed polarity. see also Figure S1.

distribution and polarity of microtubules throughout spindles, as well as the density and locations of microtubule plus ends and minus ends. We used this method to characterize microtubules in metaphase spindles assembled in *Xenopus laevis* egg extracts. We discovered a complex organization in these spindles, in which microtubules are shortest at poles and progressively increase in length toward the center of the spindle. These structural data, in combination with biochemical perturbations, fluorescence optical imaging, and mathematical modeling, support a model in which the internal architecture of the spindle arises from the spatial profile of nucleation in combination with local sorting of microtubules by transport.

RESULTS

Laser Ablation Induces Synchronous Depolymerization of Microtubules in Spindles

We used a pulsed amplified femtosecond laser to cut microtubules in metaphase-arrested spindles assembled in *Xenopus laevis* egg extracts (Hannak and Heald, 2006; Murray, 1993). As opposed to mechanical cutting techniques or long-pulsed laser severing, femtosecond laser ablation can be used to perform very accurate and selective surgery in the sample bulk with energies of only a few nanojoules (Heisterkamp et al., 2005). We cut thin, rectangular regions, typically 20 × 2 × 0.1 μm^3 (Figure 1A). These cuts induce a rapid, synchronous depolymerization of microtubules that propagates toward the poles (Figure 1B; Movie S1 available online). After approximately 1 min, the spindles completely recover to their previous state, showing no signs of damage. When microtubules are cut in vitro (Walker et al., 1989) or in interphase cells (Khodjakov et al., 2004; Botvinick et al., 2004; Colombelli et al., 2005), the newly generated plus ends rapidly depolymerize, whereas the newly generated minus ends remain stable, and strong arguments have been made that the same phenomenon occurs in spindles (Inoué, 1964; Forer, 1965; Spurck et al., 1990; Leslie and Pickett-Heaps, 1984; Maiato et al., 2005; Tirnauer et al., 2004; Nicklas et al., 1989). Cutting individual polarity-marked microtubules and polarized arrays of microtubules in extract confirms that cut microtubules depolymerize from the newly generated plus ends (see Extended Experimental Procedures and Figure S1). We therefore interpret the waves of microtubule depolymerization as coming from depolymerizing newly generated microtubule plus ends produced by the laser cut (Figures 1C and S1).

We quantified the rate of microtubule depolymerization after a cut by numerically calculating the time derivative of the intensity at each pixel of the images in the time-lapse movies (Figures 1B and S3; Movie S1). This procedure shows that depolymerization occurs in two narrow fronts perpendicular to the long axis of the spindle (Figure 2A; Movie S2), which can be conveniently visualized by integrating the depolymerization in the perpendicular direction to the spindle axis and plotting the fronts on a one-dimensional graph (Figures 2B and S3). The fronts propagate toward the poles at a constant velocity (Figure 2B, insert), with an average speed of 34.7 ± 1.7 μm/min, corresponding to the microtubule depolymerization velocity. The images of the propagating fronts of depolymerization (Figure 2A) are reminiscent of data from tubulin photoactivation experiments (Sawin and Mitchison, 1991), but these two measurements are fundamentally different as photoactivation is used to visualize marked tubulin in the microtubule lattice, whereas the fronts are direct measures of microtubule depolymerization.

The Asymmetry in the Depolymerization Fronts Reveals the Polarity of Microtubules in Spindles

The total amount of microtubule depolymerization immediately after the cut is typically different for the two depolymerization fronts that are created (Figure 2B, blue curve—the area under the two peaks is different). As depolymerization after a cut is due to newly generated plus ends (see above), this asymmetry in microtubule depolymerization is caused by a different number

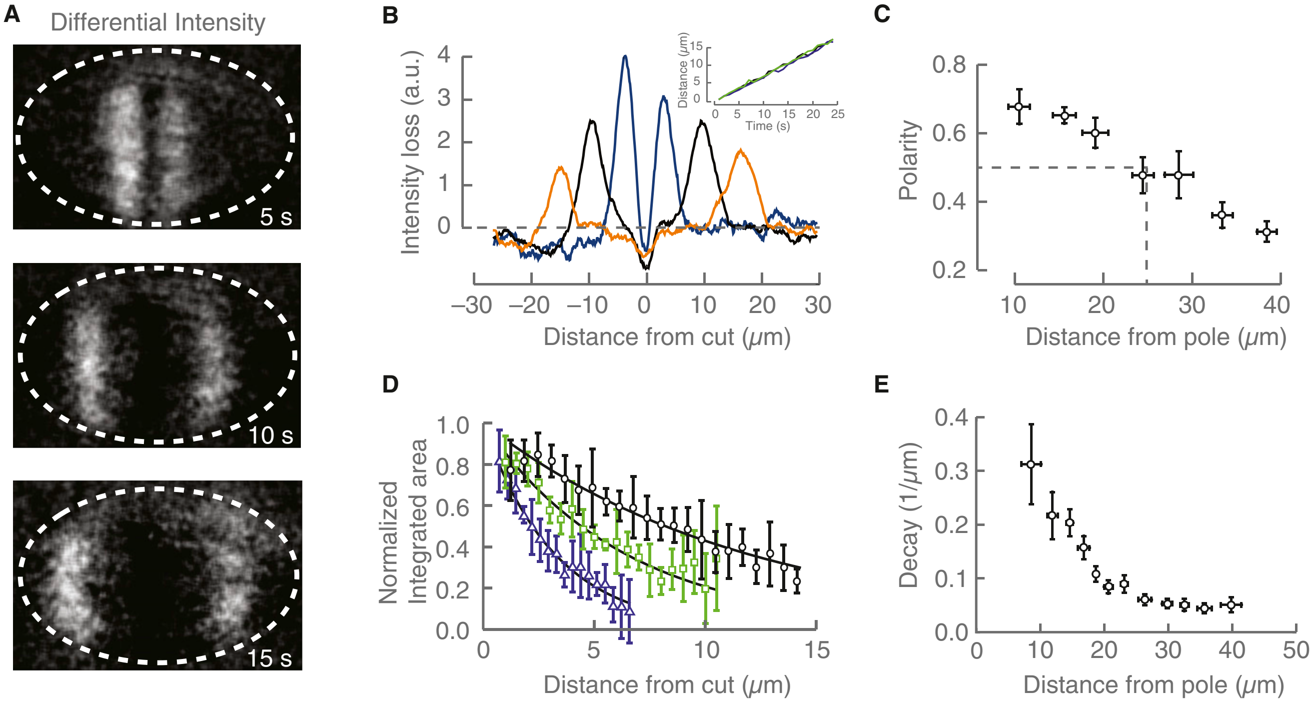

Figure 2. Characterization of the Fronts of Depolymerization

(A) Rate of intensity loss 5 s, 10 s, and 15 s after the laser cut obtained by calculating the negative of the temporal derivate at each pixel of the movie corresponding to Figure 1B and applying a Gaussian filter to aid visualization. See also Movie S2.

(B) One-dimensional profile for the rate of intensity loss from Figure 2A at 5 s (blue), 15 s (black), and 25 s (orange) (see also Figure S2). Inset, trajectories of the wave front for three cuts at 8.6 μm (blue), 16.8 μm (green), and 20.7 μm (black).

(C) Spatial dependence of microtubule polarity. Error bars represent standard deviations (SD) for positions and standard errors of the mean (SEM) for polarity.

(D) Total normalized rate of intensity loss as a function of the distance from the cut and corresponding exponential fits, for cuts performed at an average of 8.6 μm (blue triangles), 16.8 μm (green squares), and 20.7 μm (black circles) from the pole toward which the front propagates. The bars are SD.

(E) Spatial variation of the decay (inverse decay length) of the depolymerization front obtained by fitting an exponential to the rate of intensity loss as a function of the distance from the cut. The bars correspond to the SD for the position and are calculated using error propagation of the error in the fit and the error in the propagation velocity of the front for the inverse decay length.

of newly generated plus ends in the two directions. Therefore, the relative ratio of the initial area under the fronts is a measure of the polarity—the fraction of microtubules pointing in one direction—at the location of the cut (see Extended Experimental Procedures). We investigate the spatial variation of polarity in the spindle by cutting a total of 36 spindles at different locations and grouping the cuts by proximity with at least 5 spindles per group (Figure 2C). In the middle of the spindle, the polarity is 0.48 ± 0.05, with equal numbers of microtubules pointing in both directions, whereas, close to a pole, the majority of microtubules are oriented with their plus ends away from the pole. These results are consistent with previous EM measurements of microtubule polarity in other spindles (Euteneuer et al., 1982; Heald et al., 1997).

The Progressive Decrease in the Depolymerization Fronts Reveals the Locations of the Minus Ends of Cut Microtubules

The area of the front of depolymerization decreases as it progresses away from a cut (Figure 2B). This decrease is not caused by photobleaching, which is negligible during the lifetime of the front (Figure S2A), and indicates that progressively fewer microtubules depolymerize as the front advances. We quantify this decrease by averaging results from different spindles cut at similar locations. The area under the front decays exponentially ($R^2 > 0.99$) for all cuts, but the length scale of this decay depends on the position of the cut (Figure 2D): fronts from cuts made near the pole exhibit a rapid decay as they propagate toward the pole, whereas fronts from cuts made far away from the pole display more gradual decays as they progress in that direction (Figure 2E).

Two different mechanisms could explain the decrease in microtubule depolymerization as the front advances: (1) cut microtubules might depolymerize all the way to their minus ends, and, if these minus ends are spread throughout the spindle, that would result in less depolymerization as the front progresses (Figure 3A, upper); (2) depolymerizing microtubules might experience rescues, converting to a nondepolymerizing state (Figure 3A, lower). The first mechanism is likely to contribute to the decrease in depolymerization because there is extensive evidence that microtubule minus ends are present throughout *Xenopus laevis* extract spindles (Burbank et al.,

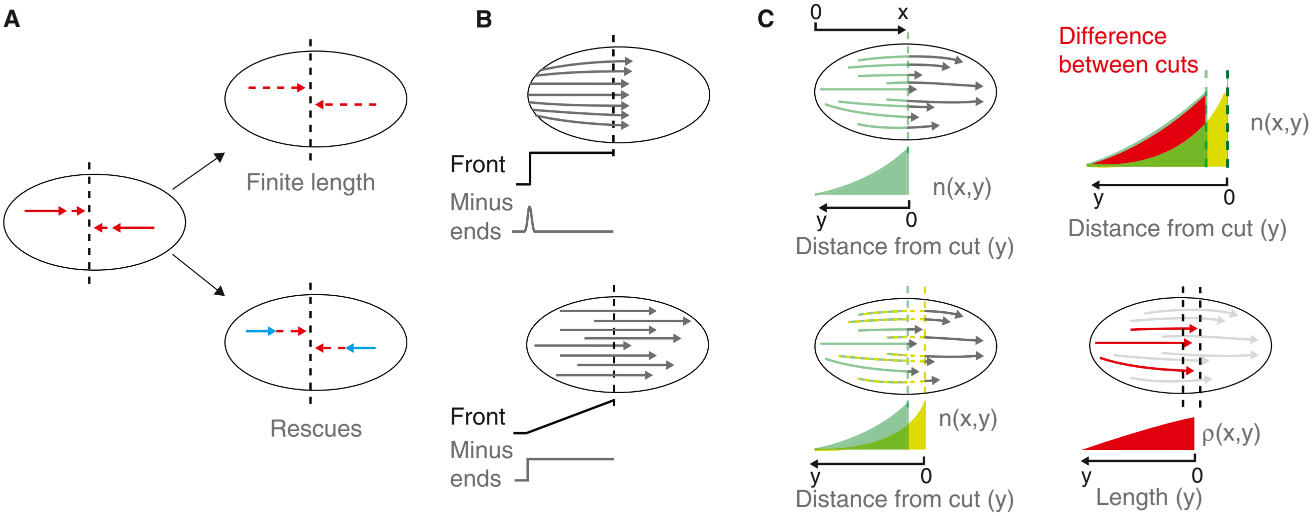

Figure 3. Using Laser Cuts to Study the Organization of Microtubules in Spindles

(A) The decrease in depolymerization as the front propagates could be caused by cut microtubules (left) either depolymerizing completely to their minus ends (upper, dotted red) or converting to a nondepolymerization state (lower, solid green). See also Figure S2.

(B) Two examples illustrating that the decay of the front depends on both microtubule organization and length. Upper: If microtubules are arranged with all minus ends at the poles, the amplitude of the depolymerization wave remains constant until reaching the pole. Lower: If microtubules of the same length are randomly arranged, the depolymerization wave decreases linearly as it approaches the pole.

(C) Graphical representation of the two-cut method for measuring microtubule lengths and organization (see also Figure S3). In this graphical representation, we only consider microtubules of one polarity. Upper left: A cut at a distance x from the pole severs microtubules that cross x (gray). These microtubules depolymerize to their minus ends, located a distance y from the cut (green), revealing the densities of minus ends $n(x,y)$, located at a distance $x - y$ from the pole, of microtubules that cross the cut at x. Lower left: A cut performed at a nearby location will typically have a different decay profile because microtubules severed by the second cut (dotted yellow) do not necessarily have the same lengths and organization as microtubules severed by the first cut (solid green). Right: The difference between the minus-end densities from the two cuts is equal to the densities of minus ends whose corresponding plus ends lie between the two cuts (red microtubules and solid red profile).

2006; Yang et al., 2007; Needleman et al., 2010). As the frequency of rescues in *Xenopus laevis* spindles has not been directly measured, we designed a method to quantify the importance of this second mechanism (see Extended Experimental Procedures). Briefly, if the decrease in depolymerization is primarily caused by rescues, then this decrease would not be changed by perturbations that increase microtubule length through a reduction in the frequency of catastrophes. Therefore, we perturbed microtubule lengths by inhibiting the protein MCAK (also referred to as XKCM1 or KIF2C), a microtubule depolymerase that increases catastrophe frequency in vivo (Walczak et al., 1996) and in vitro (Desai et al., 1999). We measured that the rate of decay of the front in these perturbed spindles is greatly reduced, showing that the rescues are negligible (see Extended Experimental Procedures). These results demonstrate that the decrease in depolymerization as the front progresses is caused by the cut microtubules depolymerizing all the way to their minus ends, which are spread throughout the spindle. Conversely, this means that the decrease in depolymerization of the advancing front provides a quantitative measure of $n(x,y)$, the density of microtubule minus ends located at a position $x - y$ from microtubules that were cut at position x (Figures 3 and S3; Extended Experimental Procedures). The dynamics of individual microtubules in these extracts suggest that the minus ends are static during the time the front propagates (see Figure S1C).

Combining Information from Two Cuts Allows a Quantitative Measure of the Length and Organization of Microtubules in Spindles

The lengths of microtubules that cross the cut cannot be inferred from the positions of their minus ends alone, as this depends on both their length and organization in the spindle (i.e., the locations of both their plus ends and minus ends). This effect is illustrated in Figure 3B, which demonstrates how microtubules with the same lengths can have minus ends at different locations and thus produce different decays.

We devised a method that uses information from multiple cuts to extract both the locations and densities of microtubule minus ends and plus ends, as well as the length distribution of microtubules at different locations in the spindle. We present an overview of the method here (Figures 3C and S3), and a more detailed derivation is given in the Extended Experimental Procedures. Consider a cut in a spindle such as in Figure 3C, upper left. We will analyze the front traveling toward the left pole, which is caused by cut microtubules whose plus ends point away from that pole. The locations and densities of the minus ends from these microtubules are specified by the decay of the front. Although the locations of their plus ends previous to the cut are unknown, these plus ends must extend past the cut. Two nearby cuts do not necessarily exhibit identical decays (Figure 3C, lower left). Indeed, from the microtubules severed by the first cut, only those whose plus ends extend past the

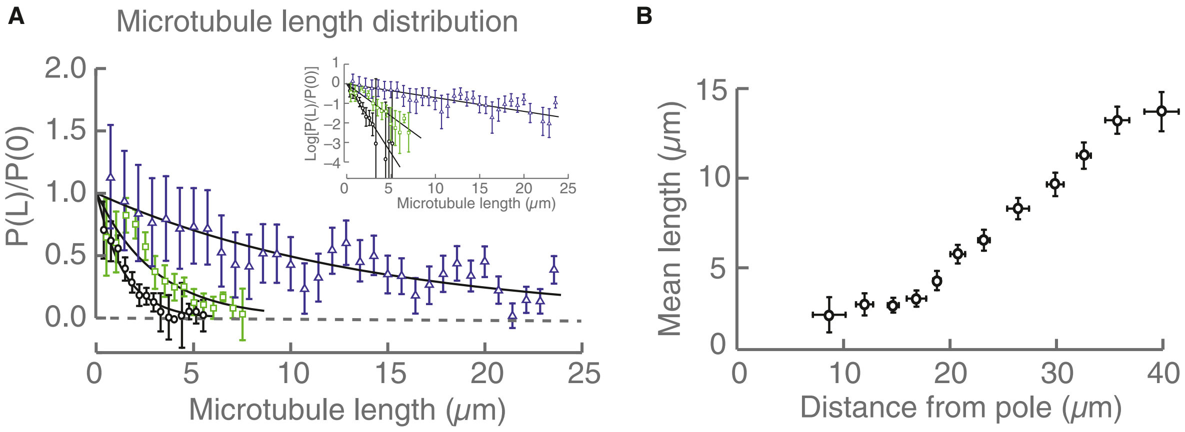

Figure 4. Microtubule Length Distributions in the Spindle

(A) Normalized probability distribution of microtubule lengths pointing away from a pole at three different distances from the pole, 8.6 μm (black circles), 16.8 μm (green squares), and 39.8 μm (blue triangles), and corresponding error bars obtained from error propagation. Solid lines correspond to exponential fits ($R^2 = 0.98$, 0.94, and 0.93, respectively). In the inset, the same data are displayed on a log-linear plot.

(B) Spatial variation of the microtubule mean length measured from their plus ends (black circles). Error bars are obtained from the SD for the position and from error propagation for the mean length.

second cut are also severed by the second cut. Therefore differences between the minus ends obtained from the two cuts correspond to those minus ends whose plus ends are located between the two cuts, i.e., those microtubules that cross the location of the first cut but not the location of the second cut (Figure 3C, right). In mathematical terms (Figure 3C and Extended Experimental Procedures), the densities of microtubules of length y whose plus ends are located at a position x, $\rho(x,y)$, are related to the densities of microtubule minus ends at a position $x - y$ from microtubules that cross a position x, $n(x,y)$, by

$$\rho(x,y) = -\left(\frac{\partial}{\partial x}+\frac{\partial}{\partial y}\right)n(x,y), \tag{1}$$

where the two partial derivatives arise because, in this coordinate system, the positions of minus ends depend on both y and x. As $n(x,y)$ can be measured from individual cuts, this equation allows us to combine information from multiple cuts on different spindles to measure the length distribution of microtubules at different locations throughout spindles, $\rho(x,y)$ (see Extended Experimental Procedures for additional information).

Numerically evaluating Equation 1 using data obtained from different cuts reveals that microtubule lengths are exponentially distributed at all locations, though their average length depends on their position in the spindle (Figure 4A). The mean length of microtubules near a pole, with their plus ends pointing away from that pole, is 2.4 ± 1.0 μm. Microtubule lengths monotonically increase away from that pole, reaching a maximum of 13.7 ± 1.1 μm (Figure 4B).

Distinguishing Mechanisms of Microtubule Length Regulation in Spindles

Why are microtubules shorter near spindle poles and longer away from them? This spatial variation in microtubule lengths must result from a spatial variation in some aspect of microtubule behavior. We consider two very general classes of models:

(1) Spatially varying microtubule stability: the increase in microtubule length away from poles might result from microtubules being selectively stabilized in the central region of the spindle (perhaps caused by proximity to chromosomes) or the destabilization of microtubules close to the poles.

(2) Spatially varying microtubule nucleation with microtubule transport: the observed differences in microtubule lengths could also arise with spatially uniform microtubule stability. If the creation of new microtubules—nucleation—is not uniform in the spindle, then microtubule transport can displace microtubules, creating a nonuniform length distribution in the spindle, which will depend on the nucleation profile and the extent of microtubule transport.

A Mathematical Model Reveals that Either Spatially Varying Nucleation or Spatially Varying Stability Could Reproduce the Measured Lengths of Microtubules

We developed a mathematical description to investigate the validity of the two models—spatially varying microtubule stability (model 1) and spatially varying microtubule nucleation with microtubule transport (model 2). Our description includes the key elements of microtubule behavior: nucleation, transport, and polymerization dynamics. Briefly, we model microtubules as polymerizing at a rate of ν_p = 10 μm/min (measured from Alexa569-EB1, data not shown, and Tirnauer et al., 2004), depolymerizing at a rate ν_d = 35 μm/min (estimated from the propagation velocity of the fronts after a laser cut), and transported toward their minus ends at a constant velocity ν_t = 2.5 μm/min (measured from speckle microscopy, data not shown, and Miyamoto et al., 2004). We characterize microtubule stabilization via a catastrophe rate γ: the rate of transitioning from the polymerizing state to the depolymerizing state. Incorporating alternative mechanisms of spatially varying stability—such as disassembly from minus ends or severing—would not substantively alter the conclusions that follow. Finally, we model the creation of new microtubules via a rate of microtubule nucleation r. We then considered two extreme limits corresponding to our two potential models: either a uniform rate of microtubule nucleation r and a spatially varying rate of catastrophe γ to represent spatially varying microtubule stability (model 1) or a spatially varying rate of nucleation and a uniform catastrophe rate to represent spatially varying microtubule nucleation (model 2).

To test these two potential scenarios, we sought to determine whether it was possible to find a profile of catastrophe (model 1) or a profile of nucleation (model 2) that could reproduce the measured variation in microtubule lengths in the spindle. We numerically fit both models to the data, keeping all other parameters fixed (Figures 5A and 5B; Extended Experimental Procedures). Both models result in good fits to the measured microtubule length distribution (Figure 5C, with $R^2 > 0.99$ for both models), indicating that either of these models could potentially account for the observed spatial variation in microtubule lengths.

Tubulin Incorporation and Polymerizing Plus Ends Are Consistent with Spatially Varying Nucleation with Microtubule Transport and Inconsistent with Spatially Varying Stability

Although both models predict similar microtubule length distributions, the underlying behaviors of microtubules that give rise to these distributions are very different. If microtubule nucleation is peaked in the center of the spindle as postulated in the spatially varying nucleation with microtubule transport model, then tubulin incorporation would be more rapid in the center of the spindle. In contrast, the spatially varying stability model predicts more rapid turnover at the poles (intuitively: in this model microtubules are shorter at poles because they are less stable there, so, if microtubule density is constant, they must turnover more rapidly at poles). We measured microtubule turnover in spindles by spiking in Atto565-labeled tubulin to previously assembled spindles in the presence of Atto488-tubulin and imaging fixed samples at various time points to follow the incorporation of new tubulin into the spindle (Figure 5D, upper) (Brown et al., 2007; Burbank et al., 2006; Needleman et al., 2010). These data indicate that tubulin becomes more rapidly incorporated in the center of the spindle and are quantitatively consistent with the predictions of the spatially varying nucleation with microtubule transport model, using the previously determined nucleation profile (compare Figure 5D, lower, gray solid lines and blue solid lines). These results are inconsistent with the spatially varying stability model, which predicts more rapid incorporation of tubulin at poles (Figure 5D, lower, dashed yellow lines).

If the spatially varying nucleation with microtubule transport model is correct, an increased rate of microtubule nucleation in the center of the spindle would result in a higher density of growing plus ends at the center compared to the poles. In contrast, the spatially varying stability model predicts a more uniform density of growing plus ends (arising from the constant nucleation rate and the addition of growing microtubules of both polarities). We measured the densities of growing plus ends in spindles using fluorescently labeled EB1 (Alexa568-EB1), a +TIP protein that selectively labels growing plus ends (Tirnauer et al., 2004). As observed previously (Tirnauer et al., 2004), we found that EB1, and thus growing plus ends, is enriched in the center of the spindle (Figure 5E, upper). These results are quantitatively consistent with the predictions of the spatially varying nucleation model using the previously determined nucleation profile (compare Figure 5E, lower, gray solid lines and blue solid lines) but are inconsistent with predictions from the spatially varying stability model (Figure 5E, lower, dashed yellow lines).

Inhibition of Microtubule Transport by Doubly Inhibiting Kinesin-5 and Dynein Homogenizes Microtubule Lengths, as Predicted by the Spatially Varying Nucleation with Microtubule Transport Model

The spatially varying nucleation with microtubule transport model also explains the experimentally determined densities of plus ends and the ratio of the number of plus ends to the number of minus ends in different regions of the spindle (Figure 5F; Extended Experimental Procedures). Therefore, all of our measurements are consistent with spatially uniform microtubule stability and a spindle architecture that results from a combination of microtubule transport and a nucleation profile that is enriched in the middle of the spindle (Figure 5G). Spatially uniform microtubule stability implies that, if we follow an individual microtubule in the spindle during its lifetime, its mean length would be the same regardless of its location in the spindle, given that microtubule dynamic properties are uniform in the spindle. The core of the nucleation and transport model is that transport from different spindle locations of microtubules, whose relative amounts are given by the spatially varying nucleation profile, contributes to the microtubule length distribution at any location in the spindle. A strong prediction of the model is that decreasing the rate of transport reduces the mixing of microtubules and homogenizes the length distribution throughout the spindle. As the minus ends of microtubules remain immobile when transport is impaired, the model predicts that the mean length of microtubules as measured from their minus ends—i.e., the length of microtubules whose minus ends are at a certain location in the spindle—corresponds to the length of an individual microtubule and is constant throughout the spindle because the polymerization dynamics and stability of microtubules are uniform. To test this prediction, we assembled spindles and simultaneously inhibited kinesin-5, by adding 200 μM of monastrol (Groen et al., 2008), and dynein, by adding 2 μM of P150-CC1 (Gaetz and Kapoor, 2004). Such doubly inhibited spindles have a bipolar structure with focused poles but a greatly reduced speed of microtubule transport (Miyamoto et al., 2004) of 0.6 ± 0.2 μm/min compared to the 2.3 ± 0.4 μm/min in unperturbed spindles in our experiments (measured by speckle microscopy; data not shown). Cutting such structures reveals that the organization of their microtubules is drastically different from that in control spindles. The decay length no longer decreases near the poles but is spatially uniform and equal to the longest decay length measured in control spindles (Figure 6A). To further investigate whether the increase on decay length results from the inhibition of dynein or from inhibiting microtubule transport, we assembled dynein-inhibited spindles

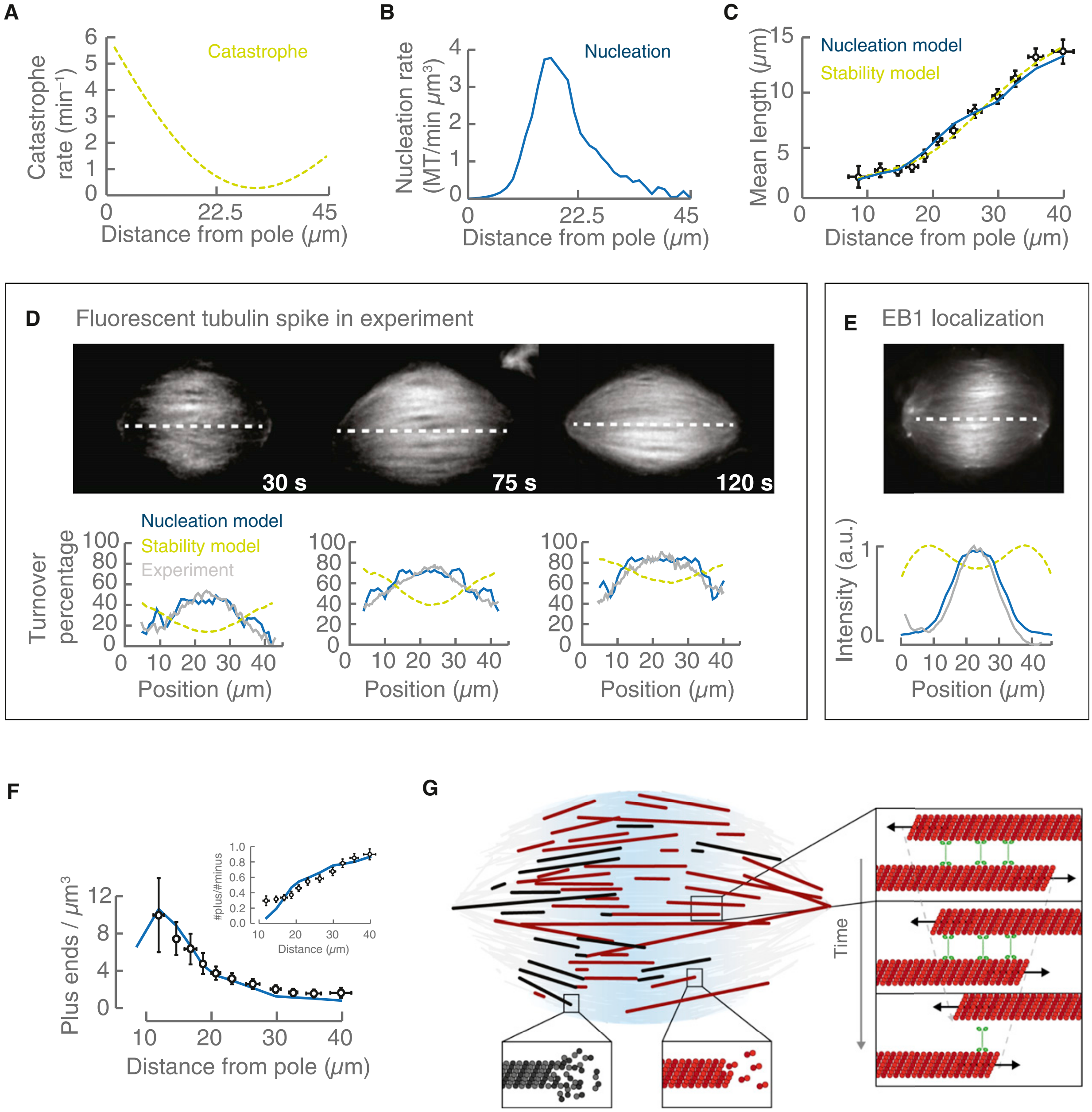

Figure 5. Verification of the Nucleation and Transport Model for Microtubule Length Regulation in the Spindle

(A–C) Profile of catastrophe rate (A, green dashed) and nucleation rate (B, solid blue) obtained by fitting the measured length distribution (C).

(D) Atto565-tubulin images of turnover measurements at 30 s (upper left), 75 s (upper middle), and 120 s (upper right), after adding Atto565-tubulin to spindles previously assembled in the presence of Atto488-tubulin. Lower: Normalized line-scan intensity profiles—Atto565-tublin intensity divided by the reference Atto488-tubulin intensity—(gray solid) corresponding to the white dashed line in upper images, and their predictions for the stabilization (dashed green) and nucleation (blue solid) models.

(E) Growing plus ends labeled with Alexa568-EB1 (upper). Lower: Intensity profile (gray solid), corresponding to the white dashed line in the upper image, and predictions from the stabilization (dashed green) and nucleation (blue solid) models. The curves from stabilization and nucleation were normalized so that their maximum intensity corresponds to the maximum of the Alexa568-Eb1 intensity profile.

(F) Densities of plus ends as a function of the distance from the poles, for microtubules pointing away from the pole, measured using the two-cut method (black circles) and prediction from the nucleation model (blue solid). Inset: Ratio of plus to minus ends as a function of distance from the pole for microtubules pointing away from the pole (solid black) and prediction from the nucleation model (blue solid). The bars correspond to the SD for the position and are calculated using error propagation for the plus-end density and for the ratio of plus-end to minus-end density.

(G) Prediction of the spindle architecture obtained from the nucleation and transport model. A small fraction of microtubules are highlighted for illustration purposes. Red lines correspond to polymerizing microtubules, and black lines to depolymerizing microtubules. Right: Microtubules of opposed polarity (arrows) slide by the action of molecular motors (green) generating a poleward transport.

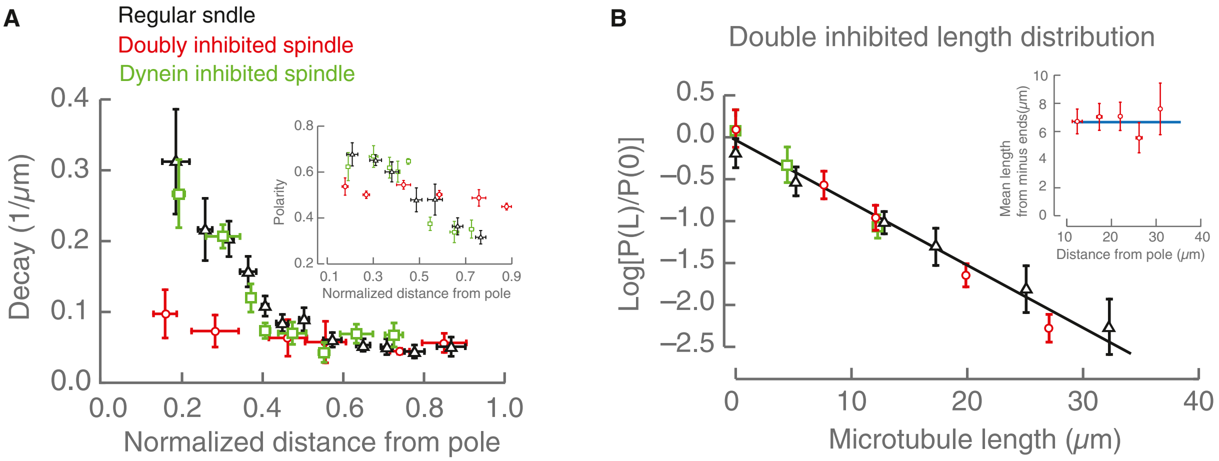

Figure 6. Inhibition of Microtubule Transport Homogenizes Microtubule Lengths in Accordance with the Nucleation and Microtubule Transport Model

(A) Comparison of front decays propagating toward a pole at *x = 0* and microtubule polarity (inset) for regular spindles (black triangles), dynein-inhibited spindles (green squares), and double-inhibited spindles (red circles) as a function of relative location in the spindle (distance from pole divided by total length of the spindle). See also Figure S5.

(B) Length distribution for microtubules in double-inhibited spindles with minus ends located at 10.4 ± 1.5 μm (black triangles), 17.2 ± 0.8 μm (red circles), and 23.7 ± 0.5 (green triangles) and exponential fit (solid black) (see also Figure S5). Error bars obtained from error propagation. Inset: Mean microtubule lengths from the minus ends (red circles) for double-inhibited spindles compared with the prediction from the nucleation and microtubule transport model (blue solid line), as a function of the distance from the pole at *x = 0*. The mean microtubule lengths in double-inhibited spindles are comparable to mean microtubule lengths from microtubules grown out of *Tetrahymena* pellicles. See Figure S4.

by adding 2 μM of P150-CC1. These spindles are longer than control spindles (66 ± 9 μm), but their decay profiles as a function of the normalized length from the spindle pole are indistinguishable from those in control spindles and markedly different from those in doubly inhibited structures (Figure 6A). This finding suggests that the difference in decays in the doubly inhibited spindles is a genuine effect of microtubule transport impairment.

The resulting reorganization in these structures is most clearly illustrated by plotting the lengths of microtubules from their minus ends (Extended Experimental Procedures), which, in the absence of transport, are predicted to be exponentially distributed with a mean length of $v_p/\gamma \approx 6.6$ μm in all regions of the spindle. Experimentally, we observed that microtubule distribution lengths from the minus ends become uniform throughout the spindle, with a mean length of 6.8 ± 1.1 μm (Figure 6B), in agreement with our predictions. This double-inhibition experiment confirms a highly nontrivial prediction of the spatially varying nucleation with microtubule transport model, providing further support for its validity.

Our results show that microtubule stability in the spindle is spatially uniform, but they do not exclude a possible global change in microtubule polymerization dynamics inside the spindle environment. If microtubules in spindles are stabilized, then they should be longer than microtubules outside of spindles. We investigated the validity of this hypothesis by studying the lengths of microtubules far removed from spindles. We used *Tetrahymena* pellicles, which can nucleate thousands of microtubules (Euteneuer and McIntosh, 1980; Coue et al., 1991), to generate dense arrays of microtubules in *Xenopus laevis* extracts (Needleman et al., 2010). Laser cuts of microtubules away from the center of these structures produce decays that are equal to the longest observed in spindles, 0.049 ± 0.004 μm^{-1} and 0.051 ± 0.014 μm^{-1}, respectively (Figure S4). We applied the two-cut method to pellicles (which lack microtubule transport) and found that the lengths of microtubules from their minus ends are homogeneous in these structures (Figure S4), with a mean length of 6.9 ± 1.8 μm, very similar to the lengths of microtubules nucleated from centrosomes in these extracts, measured by Tournebize et al. (2000) (6.3 ± 3.2 μm). Microtubule lengths in control spindles are spatially inhomogeneous due to transport, but the mean length in doubly inhibited spindles, where transport is perturbed, is 6.8 ± 1.1 μm, similar to the predicted length of microtubules in a spindle in the absence of transport, $\nu_p/\gamma \approx 6.6$ μm. Therefore, the lengths of microtubules in the spindle are the same as the lengths of microtubules outside the spindle (nucleated from pellicles or centrosomes), arguing that microtubules are not stabilized (or destabilized) by the spindle environment.

DISCUSSION

The method we present for measuring the lengths and organization of microtubules in spindles uses femtosecond laser ablation and fluorescence optical microscopy. In theory, EM could be used to obtain similar structural information, but that technique is extremely labor intensive, and only small spindles from unicellular organisms have been totally reconstructed so far. The speed and simplicity of our method allow us to quantitatively measure the organization of microtubules in several *Xenopus laevis* egg extract spindles, which have volumes tens of thousands of times larger than spindles whose structures have been previously solved by EM, and we were able to explore how the architecture in these spindles changes in response to biochemical perturbations.

Our observations that microtubule lengths are broadly distributed with their minus ends and plus ends spread throughout the *Xenopus laevis* egg extract spindles are qualitatively similar to previous indirect measurements in this system (Yang et al., 2007; Burbank et al., 2006), as well as partial EM observations in other large spindles (Mastronarde et al., 1993; Srayko et al., 2006). However, we were able to quantitatively measure the spatial variation in microtubule lengths in the spindle as well as microtubule polarity, and densities of minus ends and plus ends, enabling us to perform detailed tests of mathematical models of spindle organization. Our results show that spindles are made of microtubules that are not selectively stabilized—i.e., each individual microtubule has the same average length regardless of its position in the spindle (averaged over its lifetime)—but their organization in the spindle results in spatially inhomogeneous lengths, with the shortest microtubules found at the poles. This microtubule organization is mediated by spatial variation of nucleation and local sorting of microtubules via microtubule transport. We found that the mean length of microtubules from their minus ends is 6.8 ± 1.1 μm when transport is inhibited in spindles (Figure 6B), which is indistinguishable from the predictions of our model ($\sim$6.6 μm), our measurements on microtubules nucleated off of *Tetrahymena* pellicles (6.9 ± 1.8 μm), and previous direct measurements of the lengths of microtubules grown off of centrosomes in these extracts by Tournebize et al. (2000) (6.3 ± 3.2 μm). These results further argue that microtubule stability is not spatially regulated in spindles, in agreement with previous single-molecule measurements that established that the residency times of tubulin in microtubules are not altered by the spindle environment (Needleman et al., 2010) (though that study incorrectly concluded that the mean length of microtubules was 3 μm, as observed in a different extract system).

Previous works arguing that microtubules may be stabilized near chromatin were based on studying microtubules outside of spindles in the presence of constitutively active RAN (Athale et al., 2008; Carazo-Salas et al., 2001; Caudron et al., 2005), which might not represent the native activity of RAN on nonkinetochore microtubules in spindles or might only apply during the onset of spindle assembly, instead of the fully assembled spindles that we study here. Our structural data do not cover the regions within a few micrometers of the poles, so it is possible that the behavior of microtubules very near poles is different from that of the rest of the spindle (Loughlin et al., 2010). Our model also does not take into account the known decrease in microtubule transport close to poles (Burbank et al., 2007; Yang et al., 2008), but inclusion of this decrease would not significantly change any of our conclusions.

Our model is reminiscent of the slide-and-cluster model proposed by Burbank et al. (2007), but the role of microtubule nucleation and transport is different in these two models. Our results suggest that the spindle length is controlled by the profile of microtubule nucleation, whereas microtubule transport only locally sorts microtubules, determining their proper organization in the spindle—polarity, location, and length—without moving them appreciable distances. In contrast, in the slide-and-cluster model, microtubules are envisioned to nucleate exclusively in the center of the spindle and slide all the way to the pole, and so, in this model, the length of the spindle is determined by the distance a microtubule slides before it depolymerizes. The slide-and-cluster model is difficult to reconcile with previous results showing that a typical microtubule in the spindle is expected to move only $\sim$1 μm before it depolymerizes, because of its rapid turnover ($\sim$20 s lifetime) and slow movement ($\sim$2.5 μm/min) (Needleman et al., 2010), or with perturbations that strongly inhibit the speed of microtubule transport without significantly modifying spindle length (Ganem et al., 2005; Miyamoto et al., 2004).

What is the biological function of the complex architecture in metaphase spindles that we observe? We speculate that the inhomogeneous organization of microtubules may act as a scaffold to correctly position components in the spindle. For example, +TIPs and other proteins that bind growing microtubules naturally accumulate in the center of the spindle, which may be important for their function in anaphase. Additionally, the internal organization of microtubules may locally regulate forces on chromosomes during congression and anaphase.

Our data do not directly address the microscopic mechanism responsible for establishing the microtubule nucleation profile and are qualitatively consistent with either a gradient of nucleation around chromatin—perhaps mediated by RAN (Karsenti and Vernos, 2001) or the chromosomal passenger complex (Sampath et al., 2004)—or microtubule-mediated microtubule nucleation (Clausen and Ribbeck, 2007)—consistent with proposals for the function of augmin (Goshima et al., 2008) and the chromosomal passenger complex (Tseng et al., 2010). Interestingly, the nucleation profile resulting from our model (Figure 5B) is not symmetrical for microtubules of the same polarity (though the total nucleation profile including both polarities is symmetrical; see Figure 5E), which suggests that nucleation may depend on microtubule polarity. Although further work will be required to establish the relative contributions of different nucleation pathways, our two-cut method opens up the possibility of answering these questions by combining simultaneous measurements of both global morphological aspects and detailed local structural properties of the spindle under perturbations.

EXPERIMENTAL PROCEDURES

Spindle Assembly and Perturbations from *Xenopus laevis* Egg Extracts

Cytostatic factor (CSF)-arrested egg extracts were prepared from *Xenopus laevis* female oocytes as described previously (Hannak and Heald, 2006; Murray, 1993). Briefly, demembrenated sperm and calcium were added to extracts, resulting in the formation of nuclei. The reactions where then driven into metaphase by addition of CSF-arrested extract, and spindles formed after 1 hr at 20°C. MCAK-inhibited spindles were assembled by adding 50 μg/ml of MCAK antibodies during spindle assembly. Dynein-inhibited and Double-inhibited spindles were assembled by adding 2 μM p150-CC1 and 2 μM p150-CC1 and 200 μM monastrol, respectively, during spindle assembly. *Tetrahymena* pellicles were purified following (Coue et al., 1991).

Microscopy and Image Analysis

We used either a Nikon wide field or spinning disk confocal microscope (Nikon Ti2000, Yokugawa CSU-X1), a EMCCD camera (Hamamatsu), and a 60× objective for image acquisition. The microscope room was maintained at 20°C during experiments. Movies were taken either with the Nikon Elements software or MetaMorph (Molecular Devices). Each movie was analyzed using Matlab (The MathWorks) and Wolfram Mathematica custom-built macros.

Laser-Ablation Procedure

The femtosecond laser is composed of a mode-locked oscillator delivering 100 fs pulses at a repetition rate of 80 MHz and a central wavelength of 790 nm, followed by a chirped pulse amplification. The output pulses were delivered at a repetition rate of 10 kHz and attenuated to 2 nJ. The laser beam was coupled into the microscope and tightly focused by a 60× 1.4 NA water-immersion objective. The sample was mounted on a stage that can position it in 3D with submicrometer precision. We performed the plane-like cuts by cutting several lines spaced by 0.5 μm along the out-of-plane direction. We adapted the size and geometry of the cut to the shape and size of each spindle. The total duration of a cut was typically 4 s.

Flux, Turnover, and Plus-End Density Measurements

We measured microtubule transport velocity on regular and double-inhibited spindles by using cross-correlations on spindles with 0.5 nM Atto565-tubulin (Burbank et al., 2006). We measured tubulin turnover by adding 0.5 μM Atto565-labeled tubulin to previously assembled spindles in the presence of 0.5 μM Atto488-tubulin. Immediately after adding Atto565-tubulin, we fixed samples every 15 s and imaged afterwards. Alexa568-EB1 was added to previously assembled spindles at a final concentration of 0.1 mg/ml to measure growing plus-end density.

Simulations

Two-state microtubule dynamics were simulated using Processing (http://processing.org). Nucleation and catastrophe events were modeled as Poisson processes.

SUPPLEMENTAL INFORMATION

Supplemental Information includes Extended Experimental Procedures, five figures, and two movies and can be found with this article online at doi:10.1016/j.cell.2012.03.027.

ACKNOWLEDGMENTS

We thank Tim Mitchison for advice; Martin Wuehr, Ryoma Ohi, and Marija Zanic for providing us with P150-CC1, MCAK antibodies, and GFP-EB1, respectively; Ramon Xulvi-Brunet for useful discussions on error estimation and numerical fits; and Simone Reber, Tim Mitchison, Philippe Cluzel, Reza Farhadifar, Pierre Sens, and Bodo Stern for valuable comments on the manuscript. This work was supported by Nation Science Foundation grants PHY-0847188, DMR-0820484, CBET-0854288 and PHY-0555583 and a fellowship (to J.B.) from the Human Frontiers Science Program.

Received: August 17, 2011
Revised: November 27, 2011
Accepted: March 16, 2012
Published: April 26, 2012

REFERENCES

Athale, C.A., Dinarina, A., Mora-Coral, M., Pugieux, C., Nedelec, F., and Karsenti, E. (2008). Regulation of microtubule dynamics by reaction cascades around chromosomes. Science *322*, 1243–1247.

Botvinick, E.L., Venugopalan, V., Shah, J.V., Liaw, L.H., and Berns, M.W. (2004). Controlled ablation of microtubules using a picosecond laser. Biophys. J. *87*, 4203–4212.

Brown, K.S., Blower, M.D., Maresca, T.J., Grammer, T.C., Harland, R.M., and Heald, R. (2007). Xenopus tropicalis egg extracts provide insight into scaling of the mitotic spindle. J. Cell Biol. *176*, 765–770.

Burbank, K.S., Groen, A.C., Perlman, Z.E., Fisher, D.S., and Mitchison, T.J. (2006). A new method reveals microtubule minus ends throughout the meiotic spindle. J. Cell Biol. *175*, 369–375.

Burbank, K.S., Mitchison, T.J., and Fisher, D.S. (2007). Slide-and-cluster models for spindle assembly. Curr. Biol. *17*, 1373–1383.

Carazo-Salas, R.E., Gruss, O.J., Mattaj, I.W., and Karsenti, E. (2001). Ran-GTP coordinates regulation of microtubule nucleation and dynamics during mitotic-spindle assembly. Nat. Cell Biol. *3*, 228–234.

Caudron, M., Bunt, G., Bastiaens, P., and Karsenti, E. (2005). Spatial coordination of spindle assembly by chromosome-mediated signaling gradients. Science *309*, 1373–1376.

Clausen, T., and Ribbeck, K. (2007). Self-organization of anastral spindles by synergy of dynamic instability, autocatalytic microtubule production, and a spatial signaling gradient. PLoS ONE *2*, e244.

Colombelli, J., Reynaud, E.G., and Stelzer, E.H.K. (2005). Subcellular nanosurgery with a pulsed subnanosecond UV-A laser. Med. Laser Appl. *20*, 217–222.

Coue, M., Lombillo, V.A., and McIntosh, J.R. (1991). Microtubule depolymerization promotes particle and chromosome movement in vitro. J. Cell Biol. *112*, 1165–1175.

Desai, A., Verma, S., Mitchison, T.J., and Walczak, C.E. (1999). Kin I kinesins are microtubule-destabilizing enzymes. Cell *96*, 69–78.

Ding, R., McDonald, K.L., and McIntosh, J.R. (1993). Three-dimensional reconstruction and analysis of mitotic spindles from the yeast, Schizosaccharomyces pombe. J. Cell Biol. *120*, 141–151.

Dumont, S., and Mitchison, T.J. (2009). Force and length in the mitotic spindle. Curr. Biol. *19*, R749–R761.

Euteneuer, U., and McIntosh, J.R. (1980). Polarity of midbody and phragmoplast microtubules. J. Cell Biol. *87*, 509–515.

Euteneuer, U., Jackson, W.T., and McIntosh, J.R. (1982). Polarity of spindle microtubules in Haemanthus endosperm. J. Cell Biol. *94*, 644–653.

Forer, A. (1965). Local reduction of spindle fiber birefringence in living Nephrotoma suturalis (Loew) spermatocytes induced by ultraviolet microbeam irradiation. J. Cell Biol. *25*, 95–117.

Gaetz, J., and Kapoor, T.M. (2004). Dynein/dynactin regulate metaphase spindle length by targeting depolymerizing activities to spindle poles. J. Cell Biol. *166*, 465–471.

Ganem, N.J., Upton, K., and Compton, D.A. (2005). Efficient mitosis in human cells lacking poleward microtubule flux. Curr. Biol. *15*, 1827–1832.

Greenan, G., Brangwynne, C.P., Jaensch, S., Gharakhani, J., Jülicher, F., and Hyman, A.A. (2010). Centrosome size sets mitotic spindle length in *Caenorhabditis elegans* embryos. Curr. Biol. *20*, 353–358.

Groen, A.C., Needleman, D., Brangwynne, C., Gradinaru, C., Fowler, B., Mazitschek, R., and Mitchison, T.J. (2008). A novel small-molecule inhibitor reveals a possible role of kinesin-5 in anastral spindle-pole assembly. J. Cell Sci. *121*, 2293–2300.

Goshima, G., and Scholey, J.M. (2010). Control of mitotic spindle length. Annu. Rev. Cell Dev. Biol. *26*, 21–57.

Goshima, G., Mayer, M., Zhang, N., Stuurman, N., and Vale, R.D. (2008). Augmin: a protein complex required for centrosome-independent microtubule generation within the spindle. J. Cell Biol. *181*, 421–429.

Hannak, E., and Heald, R. (2006). Investigating mitotic spindle assembly and function in vitro using Xenopus laevis egg extracts. Nat. Protoc. *1*, 2305–2314.

Heald, R., Tournebize, R., Habermann, A., Karsenti, E., and Hyman, A. (1997). Spindle assembly in Xenopus egg extracts: respective roles of centrosomes and microtubule self-organization. J. Cell Biol. *138*, 615–628.

Heisterkamp, A., Maxwell, I.Z., Mazur, E., Underwood, J.M., Nickerson, J.A., Kumar, S., and Ingber, D.E. (2005). Pulse energy dependence of subcellular dissection by femtosecond laser pulses. Opt. Express *13*, 3690–3696.

Howard, J., and Hyman, A.A. (2007). Microtubule polymerases and depolymerases. Curr. Opin. Cell Biol. *19*, 31–35.

Inoué, S. (1964). Organization and function of the mitotic spindle. In Primitive Motile Systems in Cell Biology, R.D. Allenand and N. Kamiya, eds. (New York: Academic Press Inc.), pp. 549–598.

Karsenti, E., and Vernos, I. (2001). The mitotic spindle: a self-made machine. Science *294*, 543–547.

Khodjakov, A., La Terra, S., and Chang, F. (2004). Laser microsurgery in fission yeast; role of the mitotic spindle midzone in anaphase B. Curr. Biol. *14*, 1330–1340.

Leslie, R.J., and Pickett-Heaps, J.D. (1984). Spindle microtubule dynamics following ultraviolet-microbeam irradiations of mitotic diatoms. Cell *36*, 717–727.

Loughlin, R., Heald, R., and Nédélec, F. (2010). A computational model predicts Xenopus meiotic spindle organization. J. Cell Biol. *191*, 1239–1249.

Maiato, H., Khodjakov, A., and Rieder, C.L. (2005). Drosophila CLASP is required for the incorporation of microtubule subunits into fluxing kinetochore fibres. Nat. Cell Biol. *7*, 42–47.

Mastronarde, D.N., McDonald, K.L., Ding, R., and McIntosh, J.R. (1993). Interpolar spindle microtubules in PTK cells. J. Cell Biol. *123*, 1475–1489.

McIntosh, J.R., and Landis, S.C. (1971). The distribution of spindle microtubules during mitosis in cultured human cells. J. Cell Biol. *49*, 468–497.

Miyamoto, D.T., Perlman, Z.E., Burbank, K.S., Groen, A.C., and Mitchison, T.J. (2004). The kinesin Eg5 drives poleward microtubule flux in Xenopus laevis egg extract spindles. J. Cell Biol. *167*, 813–818.

Mogilner, A., and Craig, E. (2010). Towards a quantitative understanding of mitotic spindle assembly and mechanics. J. Cell Sci. *123*, 3435–3445.

Murray, A.W. (1993). Cell cycle extracts. In Methods in Cell Biology, B.K. Kay and B. Peng, eds. (New York: Academic Press), pp. 581–605.

Needleman, D.J., Groen, A.C., Ohi, R., Maresca, T., Mirny, L., and Mitchison, T.J. (2010). Fast microtubule dynamics in meiotic spindles measured by single molecule imaging: evidence that the spindle environment does not stabilize microtubules. Mol. Biol. Cell *21*, 323–333.

Nicklas, R.B., Lee, G.M., Rieder, C.L., and Rupp, G. (1989). Mechanically cut mitotic spindles: clean cuts and stable microtubules. J. Cell Sci. *94*, 415–423.

Sampath, S.C., Ohi, R., Leismann, O., Salic, A., Pozniakovski, A., and Funabiki, H. (2004). The chromosomal passenger complex is required for chromatin-induced microtubule stabilization and spindle assembly. Cell *118*, 187–202.

Sawin, K.E., and Mitchison, T.J. (1991). Mitotic spindle assembly by two different pathways in vitro. J. Cell Biol. *112*, 925–940.

Schermelleh, L., Heintzmann, R., and Leonhardt, H. (2010). A guide to super-resolution fluorescence microscopy. J. Cell Biol. *190*, 165–175.

Spurck, T.P., Stonington, O.G., Snyder, J.A., Pickett-Heaps, J.D., Bajer, A., and Mole-Bajer, J. (1990). UV microbeam irradiations of the mitotic spindle. II. Spindle fiber dynamics and force production. J. Cell Biol. *111*, 1505–1518.

Srayko, M., O'toole, E.T., Hyman, A.A., and Müller-Reichert, T. (2006). Katanin disrupts the microtubule lattice and increases polymer number in C. elegans meiosis. Curr. Biol. *16*, 1944–1949.

Tirnauer, J.S., Salmon, E.D., and Mitchison, T.J. (2004). Microtubule plus-end dynamics in Xenopus egg extract spindles. Mol. Biol. Cell *15*, 1776–1784.

Tournebize, R., Popov, A., Kinoshita, K., Ashford, A.J., Rybina, S., Pozniakovsky, A., Mayer, T.U., Walczak, C.E., Karsenti, E., and Hyman, A.A. (2000). Control of microtubule dynamics by the antagonistic activities of XMAP215 and XKCM1 in Xenopus egg extracts. Nat. Cell Biol. *2*, 13–19.

Tseng, B.S., Tan, L., Kapoor, T.M., and Funabiki, H. (2010). Dual detection of chromosomes and microtubules by the chromosomal passenger complex drives spindle assembly. Dev. Cell *18*, 903–912.

Walczak, C.E., Mitchison, T.J., and Desai, A. (1996). XKCM1: a Xenopus kinesin-related protein that regulates microtubule dynamics during mitotic spindle assembly. Cell *84*, 37–47.

Walker, R.A., Inoué, S., and Salmon, E.D. (1989). Asymmetric behavior of severed microtubule ends after ultraviolet-microbeam irradiation of individual microtubules in vitro. J. Cell Biol. *108*, 931–937.

Winey, M., Mamay, C.L., O'Toole, E.T., Mastronarde, D.N., Giddings, T.H., Jr., McDonald, K.L., and McIntosh, J.R. (1995). Three-dimensional ultrastructural analysis of the Saccharomyces cerevisiae mitotic spindle. J. Cell Biol. *129*, 1601–1615.

Winey, M., Morgan, G.P., Straight, P.D., Giddings, T.H., Jr., and Mastronarde, D.N. (2005). Three-dimensional ultrastructure of Saccharomyces cerevisiae meiotic spindles. Mol. Biol. Cell *16*, 1178–1188.

Yang, G., Houghtaling, B.R., Gaetz, J., Liu, J.Z., Danuser, G., and Kapoor, T.M. (2007). Architectural dynamics of the meiotic spindle revealed by single-fluorophore imaging. Nat. Cell Biol. *9*, 1233–1242.

Yang, G., Cameron, L.A., Maddox, P.S., Salmon, E.D., and Danuser, G. (2008). Regional variation of microtubule flux reveals microtubule organization in the metaphase meiotic spindle. J. Cell Biol. *182*, 631–639.

Supplemental Information

EXTENDED EXPERIMENTAL PROCEDURES

Estimation of the Rescue Rate

Following a laser cut on the spindle, we observed fronts of microtubule depolymerization that are caused by the depolymerization of the newly generated plus ends. The amount of microtubule depolymerization decreases as the fronts advance, indicating that from the originally cut microtubules, progressively fewer depolymerize as the fronts advance (photobleaching during the progression of the fronts is negligible, see Figure S2A). Two possibilities may contribute to this observation:

1. Depolymerizing microtubules reach their minus ends and stop contributing to the front, which is purely a consequence of the microtubule lengths and their organization in the spindle.
2. The depolymerizing microtubules are progressively rescued, which additionally depends on the probability that a microtubule is rescued while it depolymerizes.

To evaluate the relative contribution of both cases, we need to mathematically express the number of depolymerizing microtubules at a certain distance from the cut—*N(x) P(x,y)*, with *N(x)* being the number of microtubules at the cut, and *P(x,y)* the probability that a microtubule depolymerizes to a distance *y* from the cut—as a function of both the density of microtubules, including their length distribution and organization, and a microtubule rescue rate, which is a dynamical parameter unknown a priori.

The rescue rate of a depolymerizing microtubule is the probability per unit time λ to transition from the depolymerizing to the polymerizing state. We define $\omega(t)$ as the probability density that a microtubule is rescued at t. Then the probability that a microtubule is rescued between t and $t+\delta t$, $\delta t\omega(t)$, is equal to the probability that a microtubule has not depolymerized until t, $1-\int_0^t \omega(t')dt'$, times the probability to transition from the depolymerizing to the polymerizing state during the interval δt, $\lambda\delta t$, $\delta t\omega(t)=(1-\int_0^t \omega(t')dt')\lambda\delta t$.

By differentiating this equation with respect to time, we obtain a differential equation for the rescue probability $\omega(t)$: $d\omega(t)/dt=-\lambda\omega(t)$, which implies that $\omega(t)=\lambda\exp(-\lambda t)$, assuming that the rate of rescue is not time dependent.

The number of microtubules that stop depolymerizing at a distance *y* from the cut, *N(x)P(x,y)*, is therefore the sum of two contributions:

(1) The probability that a cut microtubule is not rescued times the number of microtubules that have minus ends at a distance *y* from the cut and extend past the cut (see Figure S2B). The probability that a cut microtubule is not rescued is 1 minus the probability that a microtubule is rescued at any location between the cut and the minus end,$1-\int_0^{y/v_d}\lambda\exp(-\lambda t)dt'=\exp(-\lambda y/v_d)$. By defining the density of microtubules $\rho(x',y')$ with plus ends at a distance x' from the pole, and length y', the number of cut microtubules that have minus ends at a distance *y* from the cut and extend past the cut is the integral of the density of microtubules in which plus ends are past the cut, i.e., $x+\varepsilon$, that have minus ends located at a distance *y* from the cut, i.e., a length of $y+\varepsilon$, for any $\varepsilon>0$ (see Figure S2B). This contribution to the number of microtubules that stop depolymerizing at a distance *y* from the cut is therefore

$$\exp(-\lambda y/v_d)\int_0^\infty d\varepsilon\rho(x+\varepsilon,y+\varepsilon).$$

(2) The second contribution comes from the probability of being rescued at a distance *y* from the cut (i.e., after a time y/v_d, where v_d is the depolymerization velocity) times the number of microtubules that once cut are longer than *y*, i.e., *y*+κ, for any $\kappa>0$ (see Figure S2B). The probability of being rescued at a distance *y* from the cut is $\omega(y)=\lambda/v_d\exp(-\lambda y/v_d)$, where we have converted time to space using $\omega(y)dy=\omega(t)v_d dt$. The number of microtubules that once cut are longer than *y* are those that have plus ends past the cut, $x+\varepsilon$, and have minus ends at a larger distance than *y* from the cut, this is, microtubules larger than $y+\varepsilon$, $y+\varepsilon+\kappa$, for any $\varepsilon,\kappa>0$ (see Figure S2B). These two quantities lead to the microtubules that stop depolymerizing at a distance y from the cut due to rescues,

$$\lambda/v_d\exp(-\lambda y/v_d)\int_0^\infty d\varepsilon\int_0^\infty d\kappa\rho(x+\varepsilon,y+\varepsilon+\kappa).$$

Adding both contributions leads to the number of microtubules that stop depolymerizing at a distance *y* from the cut *N(x)P(x,y):*

$$N(x)P(x,y)=\exp(-\lambda y/v_d)\int_0^\infty d\varepsilon\rho(x+\varepsilon,y+\varepsilon)+\frac{\lambda}{v_d}\exp(-\lambda y/v_d)\int_0^\infty d\varepsilon\int_0^\infty d\kappa\rho(x+\varepsilon,y+\varepsilon+\kappa).$$

Thus, in the presence of rescues, the decay depends on both the density of minus ends and the rescue rate, and it is difficult to separate the relative contributions of these two mechanisms. However, in the hypothetical limit where microtubules are infinitely long, only rescues contribute to the decrease of depolymerization during the propagation of the front since the depolymerizing microtubules would never reach their minus ends, and $P(x,y)=\lambda/v_d\exp(-\lambda L/v_d)$.

We can lengthen microtubules in the spindle by inhibiting the protein MCAK (also referred to as XKCM1 or KIF2C), a catastrophe factor (Walczak et al., 1996; Desai et al., 1999). Upon addition of anti-MCAK in the extract, spindles become transiently thicker and denser and eventually transform to asters, which continually grow in size. Yet, microtubules in these spindles and asters are of finite length, so the presence of minus ends must contribute to the probability that a microtubule stops depolymerizing to some extent. Therefore, if we cut these structures and assume that the decay results solely from rescues, we can obtain an upper limit for the rescue rate. We compared decays resulting from cuts performed on MCAK inhibited spindles and MCAK inhibited asters with decays from cuts performed at a similar location in control spindles. In asters, we grouped the cuts performed the furthest away from the center of the aster, at 40.2 ± 1.6 μm (n = 4), and fitted the decay to an exponential, obtaining an inverse decay length of 0.0085 ± 0.0013 1/μm ($R^2 > 0.99$, see Figure S2C), corresponding to a decay length of 118 ± 18 μm, which corresponds to an upper limit of the rescue rate of $_\lambda$ = 0.50 ± 0.08 1/min. Cuts in control spindles at a comparable distance from the pole (45.2 ± 1.6) result in a decay length of 20.4 ± 3.2 μm, 5.8 ± 1.3 times smaller (see Figure S2C). In MCAK-inhibited spindles, cuts performed at 10.3 ± 0.7 μm from the pole exhibited a inverse decay length of 0.078 ± 0.045 1/μm ($R^2 > 0.99$, see Figure S2D), corresponding to a decay length of 12.7 ± 7.0 μm (of the same order than the distance of the cut to the pole), which is 4.0 ± 2.4 times bigger than the corresponding decay in control spindles (3.2 ± 0.7 μm). The increase in decay lengths from both anti-MCAK asters and anti-MCAK spindles with respect to control spindles is the same within error, arguing that microtubules in anti-MCAK spindles elongate like microtubules in anti-MCAK asters, and therefore justifying the use of anti-MCAK asters to obtain an upper bound estimate for the rescue rate in spindles.

Next, we estimated the extent to which the presence of a rescue rate of this magnitude would modify our conclusions regarding the measured microtubule lengths. If one falsely assumed that microtubules had a rescue rate of zero, when in fact the rate of rescue was equal to the determined by the upper limit of $\lambda = 0.50$ 1/min, then microtubules which were actually $L_T = 14\ \mu$m long (near the maximum microtubule length that we measured), would appear to have a length of

$$\langle L\rangle = L_T \exp(-L_T\lambda/v_d) + \int_0^{L_T} \lambda l/v_d \exp(-l\lambda/v_d)dl \approx 13.2\mu m,$$

which is approximately 5% different from their true length. The corresponding errors would be less than 2% and 1% for microtubules with lengths of 5 μm and 2 μm (corresponding to the central and polar region of the spindle). These deviations are below our experimental errors and are based on an overestimation of the rescue rate, so the effects of rescues can be safely neglected.

Derivation of the Two-Cut Method

Our method consists of two steps. First, the density of minus ends from the cut microtubules is obtained for each of the cuts (see Figure S5A); second, we combine the cuts in pairs to obtain the full microtubule density (plus-end and length distributions) from its mathematical relationship with the measured minus-end density (see Figure S5B).

We obtained the density of minus ends from the cut microtubules using the fact that the decrease in depolymerization results from cut microtubules that depolymerize to their minus ends. We quantified the rate of intensity loss by evaluating the numerical derivative using neighboring frames of the movie after a cut (see Figures S5A1 and S5A2). We defined the position of each front at a given time, t, $x_f(t)$, as the position of the peak of the profile of intensity loss (Figures S2B and S5A3) fitted to a bell shape, $A(t)\exp[-(x - x_f(t))^2/s(t)^2]$, where $A(t)$ is the amplitude and $s(t)$ is the width of the fitted bell shape. The integrated area under the peak (see Figure S5A3) is the total intensity loss per unit time, which we calculated using the amplitude $A(t)$, and the width of the fitted bell shape $s(t)$, $R(t) = \sqrt{\pi}A(t)s(t)$. The intensity lost during the interval t and $t + \delta t$, $R(t)\delta t$, is equal to the number of microtubules that depolymerize at t, $n_d(t)$, times the length of microtubules depolymerized during the interval δt, $v_d\delta t$, times the fluorescence per unit length and microtubule, σ_f:$R(t) = \sqrt{\pi}A(t)s(t) = n_d(t)v_d\sigma_f$. The number of depolymerizing microtubules, $n_d(t)$, is proportional to the product of the length of the cut (parallel to the focal plane) and the thickness of the cut (perpendicular to the focal plane, see Figure 1A). Confocal z stack movies show that the depolymerizing microtubules stay on the focal plane, so the thickness of the cut (perpendicular to the focal plane) does not play any role, and we can normalize R(t) and $n_d(t)$ by the thickness of the cut (typically 1–2 μm). Therefore, although we refer to $n_d(t)$ as number of depolymerizing microtubules, this quantity is a number per unit length, i.e., the number of microtubules per unit length in the perpendicular direction of the cut. At $t = 0$, this quantity gives the number of cut microtubules for both polarities, times a constant $v_d\sigma_f$. Taking the relative fraction of the integrated profile of intensity loss for the two fronts immediately after the cut ($t = 0$) reveals the polarity at the location of the cut (Figure 2C). The rate at which microtubules stop depolymerizing plus the rate at which depolymerizing microtubules reach a minus end is conserved: $d[n_d(t)]/dt + n(t) = 0$ (see Figure S5A4). Then, $dR(t)/dt = dn_d(t)/dt\ v_d\sigma_f = -n(t)v_d\sigma_f$ which gives for the density of minus ends:

$$n(y) = -1/\sigma_f\, dR(y)/dy,$$

where we have used as a variable the distance from the cut, y, which is related to time by the depolymerization velocity, $y = v_d t$. This density has units of microtubule per unit length squared, corresponding to unit length perpendicular to the cut and along the spindle longitudinal axis. Although the proportionality between fluorophore intensity and microtubules may vary from day to day, the density of microtubules at the center of the spindle is observed to be constant regardless of spindle width, which suggests that there is an absolute constant of proportionality between spindle width and density of microtubules, β_w. To calibrate β_w, we used EM cross-section images of *Xenopus laevis* spindles (M. Coughlin, personal communication; Heald et al., 1997) from which we obtain a microtubule density $\beta_w \sim 50$ microtubules/μm^2. We used this density at the center of the spindle to calibrate the fluorescence weighted shape (the sum of intensity over the width of the spindle at any location of the spindle). In the case of unperturbed spindles, the fluorescence intensity is nearly constant throughout the structure, so the fluorescence weighted shape is indistinguishable from the profile of the spindle, and we simply used the measured profile of the spindles, which is determined with less error than the fluorescence weighted shape. For other cases, where the density of microtubules is not constant along the spindle, such as the case of dynein-inhibited spindles or pellicles, we used the fluorescence weighted shape. We expressed the minus end density in terms of this absolute constant, β_w, equal for any spindle, using the fact that the total number of minus ends per unit length perpendicular to the cut from pole to cut adds up to the total number of cut microtubules of the corresponding polarity per unit length perpendicular to the cut, which in turn is equal to the product of the width of the spindle fluorescence weighted shape, the polarity at the cut, and the constant β_w,

$$\int_0^x n(y)dy = w(x)p(x)\beta_w,$$

where *x* is the distance of the cut from the pole, *w(x)* is the width of the spindle fluorescence shape, and *p(x)* is the polarity at the cut. The integral of the density of minus ends is $[R(0)-R(x)]/\sigma_f$, leading to the calibration of σ_f and the expression for the density of minus ends,

$$n(x,y) = \frac{\beta_w w(x)p(x)}{R(0)-R(x)}\frac{dR(y)}{dy},$$

which relates the density of minus ends with quantities measured in our experiments. For the regular spindle, the width *w(x)* was obtained from averaging 10 confocal spindle images. For the pellicles, we obtained the fluorescence radial shape by calculating the radial average intensity of the fluorescence images.

In a second step, we related the density of minus ends with the density of microtubules with plus ends at a distance x' from the pole, length y', and positive polarity, $\rho(x',y')$ (Figure S5B). This relation is obtained from the fact that the density of minus ends at a distance *y* from a cut performed at *x* results from the contribution of all microtubules that cross the cut and have their minus ends at a distance *y* from the cut. In mathematical terms, $n(x,y) = \int_0^\infty \rho(x+\eta, y+\eta)d\eta$ (see Figure S5B1). By considering the minus ends at the same location in the spindle but resulting from a cut slightly further away from the pole, $n(x+\varepsilon, y+\varepsilon) = \int_\varepsilon^\infty \rho(x+\eta, y+\eta)d\eta$ (see Figure S5B2), we can easily invert the relation between density of minus ends and microtubule density by subtracting the minus end density from the two cuts (see Figure S5B3), leading to

$$\rho(x,y) = -\left(\frac{\partial}{\partial y}+\frac{\partial}{\partial x}\right)n(x,y),$$

in the limit of $\varepsilon \to 0$. This is the density of microtubules with plus ends at a distance from the pole *x*, and length *y*, and has units of microtubule divided by length cubed, this is, microtubules per area of spindle cross-section and microtubule length. The microtubule organization can equivalently be described in terms of the density of microtubules with minus ends at a distance *x* from the poles, and length *y* (Figure 6B) by using the identity $\rho^+(x,y) = \rho^-(x-y,y)$, where +, – refer to density from plus and minus ends respectively. To obtain $\rho^-(x,y)$ purely numerically, we have to discretize the length *y* so that *x+y* correspond to locations of the cuts,$\rho^-(x,y) = \rho^+(x+y,y)$ (see Figure 6B). Alternatively, fitting of the decays as a function of the position can provide a higher resolution. The lengths obtained using both methods are equivalent, but in Figure 6B we chose only to show the pure numerical results.

Formally, the length distribution of microtubules with plus ends at a location *x* from the pole is obtained by normalizing the microtubule density to the number of microtubules at that location, $\rho_L(x,y) = \rho(x,y)/\int_0^\infty \rho(x,y)dy$, and the mean microtubule length is then obtained using $\langle L(x)\rangle = \int_0^\infty y\rho_L(x,y)dy$. In practice, we numerically evaluated these expressions and included a cut off on the maximum length of microtubules defined by the finite size of the spindle—a microtubule with plus ends at a distance *x* from the pole has a maximum length of *x*.

The sources of error in the minus end distribution *n(x,y)* arise from the fluorescence weighted shape, *w(x)*, the polarity, *p(x)*, and the rate of intensity loss *R(y)*,

$$\delta n(x,y) = n(x,y)\left(\left(\frac{\delta w(x)}{w(x)}\right)^2+\left(\frac{\delta p(x)}{p(x)}\right)^2+\left(\delta\frac{dR(y)/dy}{R(0)-R(x)}\right)^2\Bigg/\left(\frac{dR(y)/dy}{R(0)-R(x)}\right)^2\right)^{\frac{1}{2}}.$$

We used this expression to numerically calculate the error in *n(x,y)*, and propagate it to $\rho(x,y)$. Finally, for the microtubule length distribution, we determined the error using error propagation in the density of microtubules,

$$\delta\rho_L(x,y) = \left(\frac{\delta\rho^2(x,y)}{\left(\int\limits_0^x \rho(x,y)dy\right)^2}+\frac{\rho^2(x,y)\int\limits_0^x \delta\rho^2(x,y)dy}{\left(\int\limits_0^x \rho(x,y)dy\right)^4}\right)^{\frac{1}{2}},$$

where the limits of integration *(0,x)*, correspond to the minimum and maximum lengths of a microtubule with plus ends at a distance *x* from the pole. Finally, the error in the mean microtubule length is given by

$$\delta\langle L(x)\rangle = \left(\int_0^x y^2 \delta\rho_L^2(x,y)dy\right)^{\frac{1}{2}}.$$

Mathematical Model of Microtubule Nucleation, Transport, and Polymerization Dynamics

We used the two-state model of microtubule polymerization described in Dogterom and Leibler (1993) supplemented with microtubule sliding at a constant velocity, v_t, that transports microtubules toward the pole that microtubules grow away from (Figure 5G). We define $\rho_p(t,x,l)$ and $\rho_d(t,x,l)$ as the polymerizing and depolymerizing densities of microtubules with positive polarity, length l and plus ends at x, as a function of time t. The mass conservation equations for the two densities are

$$\frac{\partial\rho_p(t,x,l)}{\partial t} = -\nabla\cdot\mathbf{J}_p - r_{p\to d}\rho_p + r_{d\to p}\rho_d,$$

$$\frac{\partial\rho_d(t,x,l)}{\partial t} = -\nabla\cdot\mathbf{J}_d - r_{d\to p}\rho_d + r_{p\to d}\rho_p.$$

$\mathbf{J}_p$ and $\mathbf{J}_d$ are the flux of polymerizing and depolymerizing densities in the x-l space, and $r_{p\to d}$ and $r_{d\to p}$ are the transition rates from a polymerizing to a depolymerizing state and vice versa. We used the plus ends as a reference frame because catastrophes occur at the plus ends. In the x space, the density of polymerizing plus ends is transported at the sliding velocity, v_t, plus the polymerization velocity: $v_p - v_t$ (where we explicitly use the fact that microtubules are transported toward the pole, hence with a negative velocity $-v_t$). In the l space, the polymerization density is transported at the polymerization velocity: v_p. Thus the flux of the density of polymerizing microtubules is $\mathbf{J}_p = (v_p - v_t, v_p)\rho_p(t,x,l)$. Similarly, the flux of the density of depolymerizing microtubules is $\mathbf{J}_d = -(v_d + v_t, v_d)\rho_d(t,x,l)$. We define the transition rate from the polymerizing to the depolymerizing state as a catastrophe rate that may depend on the position in the spindle, $\gamma(x)$. Since rescues were experimentally negligible in the cutting experiments, we set the transition rate from the depolymerizing to the polymerizing state to 0.

We are interested in the stationary state solutions, i.e., $\partial\rho_p/\partial t = \partial\rho_d/\partial t = 0$, which are supplemented with the following boundary conditions: microtubules are nucleated at a rate that may depend of position, $\rho_p(x,0) = r(x)$; microtubules disappear when they depolymerize all the way to their minus ends, $\rho_d(x,0) = 0$; the density of polymerizing and depolymerizing microtubules at infinity vanishes, $\rho_p(\infty,l) = \rho_d(\infty,l) = 0$. The differential equations are analytically solvable for any functional form of the rate and catastrophe,

$$\rho_p(x,l) = r(x - (v_p - v_t)l/v_p)\exp\left(-\int_{x-(v_p-v_t)l/v_p}^{x}\gamma(z)dz\right),$$

$$\rho_d(x,l) = \int_0^\infty \rho_p(x + (v_t + v_d)\tau, l + v_d\tau)\gamma(x + (v_t + v_d)\tau)d\tau.$$

We then take the two limits corresponding to the nucleation model, $\gamma(x)$ = constant $\sim$1.5 min^{-1} (Wilde et al., 2001), and destabilization model, $r(x)$ = constant. To find the profile of nucleation rate that fit the length distribution (Figure 4B), we expressed the nucleation rate as a discrete sum of Heaviside functions, $r(x) = \sum_{i=1}^{n} a_i\Theta(x - y_i - \varepsilon)\Theta(x - y_i + \varepsilon)$, where $2\varepsilon = 0.5$ μm is the space discretization we chose, n = *100*, and y_i are equally spaced positions between the poles at x = 0 μm and x = 45 μm. This procedure, allows us to express the mean length as a sum of the ratio of two analytic functions multiplied by the rate coefficients, a_i which simplifies and speeds up the numerical fit,

$$\langle L(x,\vec{a})\rangle = \frac{\sum_{i=1}^{n} a_i(f(y_i,x,\varepsilon) - f(y_i,x,-\varepsilon)\Theta(-y_i + x - \varepsilon))\Theta(-y_i + x + \varepsilon)}{\sum_{i=1}^{n} a_i(g(y_i,x,\varepsilon) - g(y_i,x,-\varepsilon)\Theta(-y_i + x - \varepsilon))\Theta(-y_i + x + \varepsilon)},$$

$$\begin{aligned} f(y_i,x,\varepsilon) = \frac{\gamma}{v_p - v_t}\frac{1}{(v_d + v_t)\gamma^2}\Bigg((v_p - v_t)(v_p(v_d + v_t) + (v_p - v_t)v_t\gamma) - \exp\left[\frac{\gamma(y_i - x - \varepsilon)}{v_p - v_t}\right]\Big(v_p v_d(v_p - v_t + \gamma(x + \varepsilon - y_i)) \\ + v_t\left(v_t^2\gamma + v_p^2(1 + \gamma) - v_p(v_t + 2v_t\gamma - \gamma(x + \varepsilon - y_i))\right)\Big)\Bigg), \end{aligned}$$

$$g(y_i,x,\varepsilon) = \left(1 - \exp\left[\frac{\gamma(y_i - x - \varepsilon)}{v_p - v_t}\right]\right).$$

For the case of constant nucleation, the same procedure is not feasible, and we represented the catastrophe as a 4th degree polynomial. For each limit, we found the shape of the nucleation and catastrophe that best fit the mean length distribution of microtubules (Figure 5C).

SUPPLEMENTAL REFERENCES

Desai, A., Verma, S., Mitchison, T.J., and Walczak, C.E. (1999). Kin I kinesins are microtubule-destabilizing enzymes. Cell *96*, 69–78.

Dogterom, M., and Leibler, S. (1993). Physical aspects of the growth and regulation of microtubule structures. Phys. Rev. Lett. *70*, 1347–1350.

Heald, R., Tournebize, R., Habermann, A., Karsenti, E., and Hyman, A. (1997). Spindle assembly in *Xenopus* egg extracts: respective roles of centrosomes and microtubule self-organization. J. Cell Biol. *138*, 615–628.

Walczak, C.E., Mitchison, T.J., and Desai, A. (1996). XKCM1: a *Xenopus* kinesin-related protein that regulates microtubule dynamics during mitotic spindle assembly. Cell *84*, 37–47.

Wilde, A., Lizarraga, S.B., Zhang, L., Wiese, C., Gliksman, N.R., Walczak, C.E., and Zheng, Y. (2001). Ran stimulates spindle assembly by altering microtubule dynamics and the balance of motor activities. Nat. Cell Biol. *3*, 221–227.

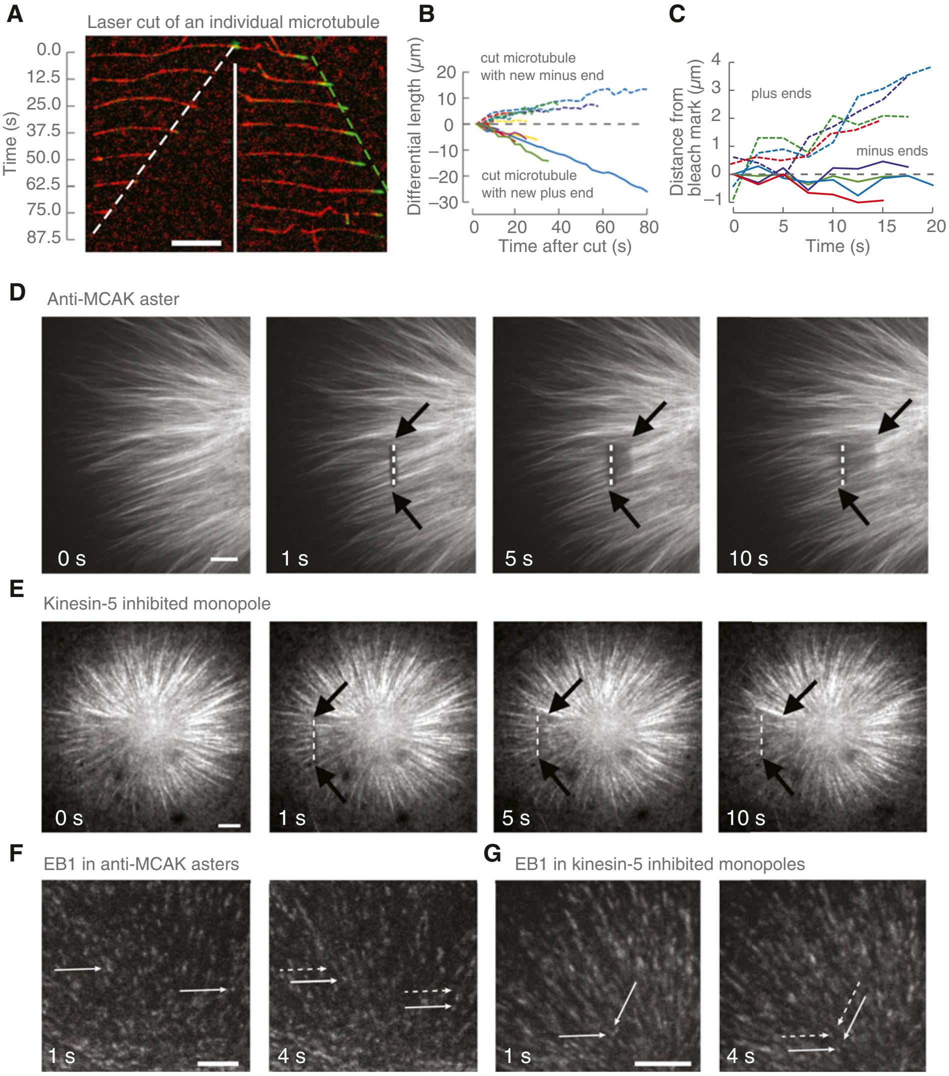

Figure S1. After a Laser Cut, Only the Newly Generated Microtubule Plus Ends Depolymerize, Related to Figure 1

(A) We added axonemes to assemble microtubules in *Xenopus* egg extracts in the absence of spindles. Individual microtubules were imaged with Atto565-labeled tubulin (red) and GFP-Eb1 (green) to mark growing plus ends and cut by laser ablation. After cutting the microtubule at *t = 0* (the green dot in the middle of the microtubule), a pair of new plus and minus ends are generated. The microtubule half with the newly generated plus end does not recruit GFP-Eb1 and depolymerizes from its plus end (white dashed line), whereas the microtubule half with the newly generated minus end remains stable and continues to grow from its plus end (green dashed line). Scale bar, 10 μm.

(B) Lengths of individual cut microtubules (n = 13) for sections with the newly generated minus ends (dashed lines) or newly generated plus end (solid lines) demonstrating that the newly generated plus ends depolymerize whereas the newly generated minus ends are stable. After a cut, 100% of depolymerization from the newly exposed ends corresponds to the plus ends. The average microtubule depolymerization rate is −22.8 ± 2.1 (SEM) μm/min, and the average microtubule polymerization rate is 12.3 ± 1.3 (SEM) μm/min.

(C) Plus-end (dashed lines) and minus-end (solid lines) dynamics of a microtubule obtained by measuring the distance of the plus ends to a reference bleach mark made on the microtubules, showing that minus ends have slow dynamics compared to the plus ends. The average velocity of the plus ends is 9.6 ± 1.1 (SEM) μm/min, and the average velocity of the minus ends is −1.2 ± 1.1 (SEM) μm/min.

(D and E) Polarized arrays of microtubules were created by (D) the addition of perturbing anti-MCAK antibodies to spindles or (E) assembling spindles in the presence of monastrol. Scale bars, 10 μm. The structures were cut by laser ablation (dashed white line) and the fronts of depolymerization were followed (black arrows). Quantification of the cuts reveals that the inward propagating front accounts for 79% ± 14% (anti-MCAK) and 82% ± 9% (monastrol) of the total depolymerization.

(F and G) Imaging growing plus ends of microtubules with GFP-EB1 in anti-MCAK asters (F) and monastrol monopoles (G) shows that most microtubules have their plus end facing away from the center of the structure, but a subset of microtubules have their plus ends in the opposite direction. Two examples of microtubules with plus ends growing to the center in both structures are marked (current and previous comet positions are indicated by white solid and dotted arrows, respectively). Quantification of these data demonstrates that 80% ± 3% for anti-MCAK asters and 81% ± 10% for monopoles of EB1 comets propagated outward, whereas the rest propagated toward the center. This is consistent with the extent of microtubule depolymerization in that direction—79% ± 14% (anti-MCAK) and 82% ± 9% (monastrol)—further arguing that cut microtubules depolymerize exclusively from their newly generated plus ends. Scale bars, 10 μm.

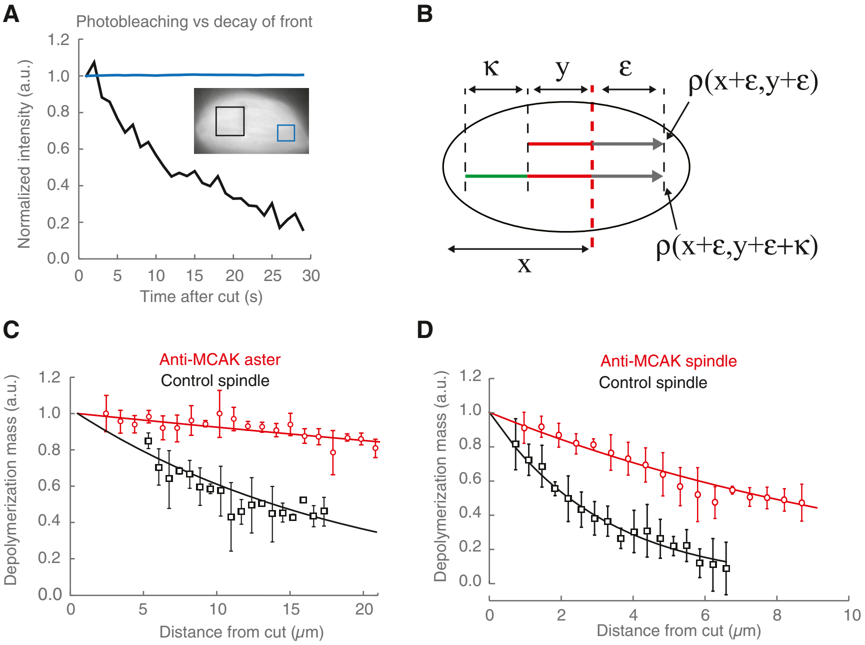

Figure S2. The Decay on the Fronts Results from the Finite Length of the Cut Microtubules, Related to Figures 2 and 3

(A) Comparison of the temporal dependence of the normalized integrated intensity profile of a front (solid black) for a cut performed in the spindle (inset, black box represents the region of depolymerization) and the normalized mean intensity (solid blue) of an uncut region in the same spindle (inset, blue square). The lack of decay in the uncut region demonstrates that photobleaching is negligible.

(B) A depolymerizing microtubule (red) cut at a distance x from the pole, with plus end originally at a distance ε from the cut, stops depolymerizing at a distance y from the cut because it either reaches its minus end (upper microtubule) or is rescued and has its minus end located a distance κ away from where it stops depolymerizing (green, lower microtubule).

(C) Depolymerization mass resulting from cuts performed in anti-MCAK asters (red circles) and control spindles (black squares) at a distance of 40.2 ± 1.6 μm and 45.2 ± 1.6 μm from the pole, respectively, and corresponding exponential fits (solid red and solid black respectively) as a function of the distance from the cut.

(D) Depolymerization mass resulting from cuts performed in spindles with anti-MCAK (red circles) and control spindles (black squares) at a distance of 10.3 ± 0.7 μm and 8.6 ± 1.5 μm from the pole, respectively, and corresponding exponential fits (solid red and solid black, respectively) as a function of the distance from the cut.

In both (C) and (D), the bars are SD.

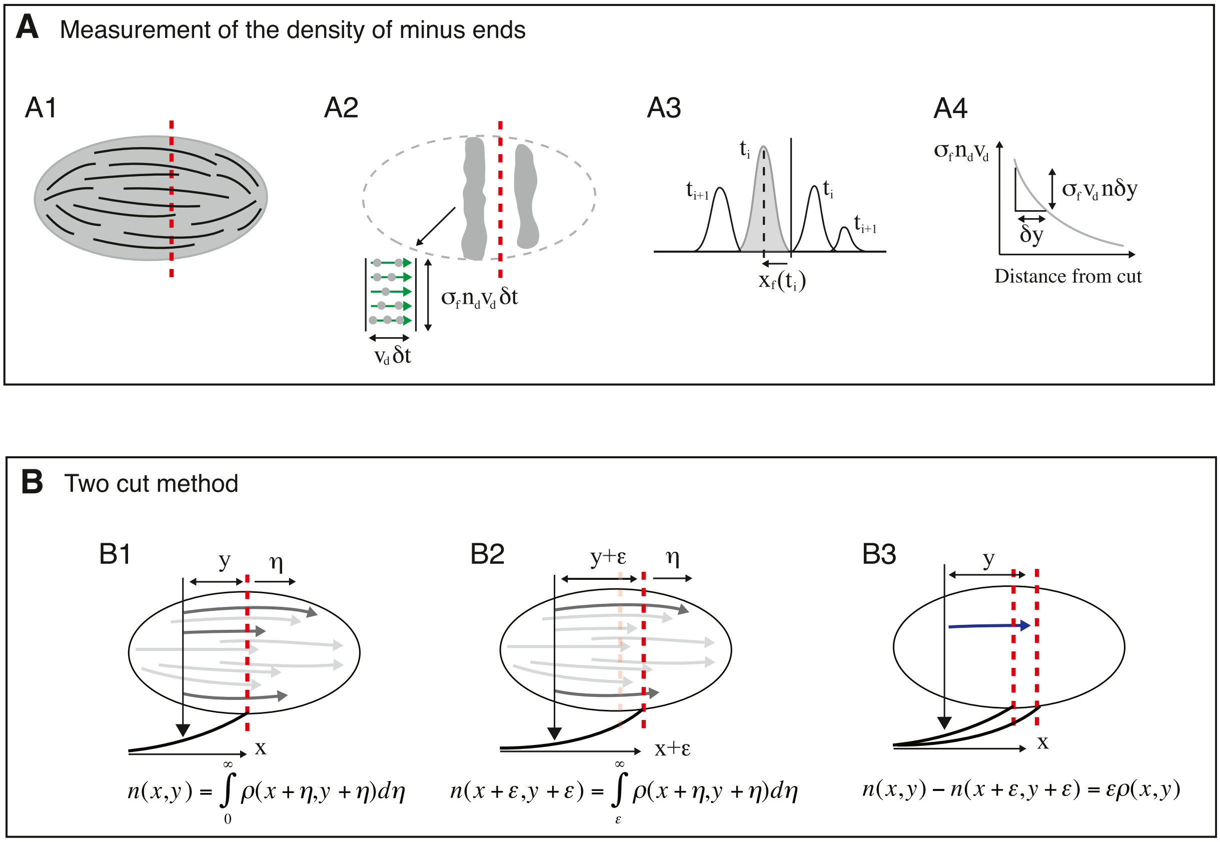

Figure S3. Graphical Representation of the Minus-End Density Measurements and the Two-Cut Method, Related to Figure 3

(A) Successive steps followed to measure the density of minus ends in the spindle. (A1) A fluorescently labeled spindle is cut (dashed red line) perpendicular to the long spindle axis. (A2) We obtain a differential intensity movie that reveals the amount of microtubule depolymerization (gray bands). When comparing two frames, the differential intensity results from the amount of depolymerized microtubules—the amount of fluorescent tubulin lost—during the time between those frames. The observed differential intensity is equal to the product of the number of cut microtubules n_d, the length of depolymerized microtubule $v_d \delta t$ (green arrows, δt being the time between frames), and the amount of fluorescent tubulin per unit microtubule length σ_f. (A3) We obtain the time derivative of the movie by dividing the differential intensity by the time between frames, and we sum intensity over the direction perpendicular to the spindle long axis. This procedure results in curves with a characteristic Gaussian profile that represent the depolymerization front and propagate over time. We use the peak of the profile to define the position of the front as a function of time $x_f(t)$, and we calculate the area under the profile (gray region) to obtain the total amount of front depolymerization as a function of the position of the front. (A4) The variation of the amount of depolymerization at a certain distance from the cut is caused by the amount of minus ends from the depolymerizing microtubules at that location.

(B) Derivation of the two-cut method. (B1) The minus ends measured at a distance y from a cut performed at a distance x from the pole $n(x, y)$ are the sum of all the microtubules that cross the cut, i.e., with plus ends at $x + \eta$, and length $y + \eta$, for any $\eta > 0$. (B2) The minus ends at the same location in the spindle resulting from a cut further away from the pole. (B3) The difference of the density of minus ends at a location in the spindle from two nearby cuts is proportional to the distance between cuts and the density of microtubules with plus ends between the cuts that extend to the location of the minus ends (blue microtubule).

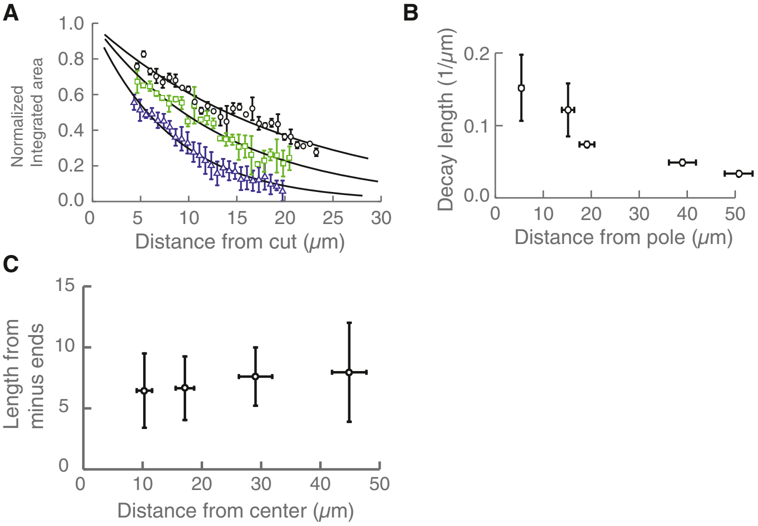

Figure S4. Characterization of Cuts from *Tetrahymena* Pellicles, Related to Figure 6

(A) Total normalized rate of intensity loss as a function of the distance from the cut and corresponding exponential fits, for cuts performed at an average of 15.2 ± 1.3 μm (blue triangles), 19.1 ± 1.6 μm, and 39.0 ± 2.8 μm (black circles) from the center of the pellicle. The bars are SD.

(B) Spatial variation of the decay (inverse decay length) of the depolymerization front obtained by fitting an exponential to the rate of intensity loss as a function of the distance from the cut. The bars correspond to the SD for the position, and are calculated using error propagation of the error in the fit and the error in the propagation velocity of the front for the inverse decay length.

(C) Mean microtubule lengths from the minus ends as a function of the distance from the pole at $x = 0$. Error bars are obtained from the SD for the position and from error propagation for the mean length.

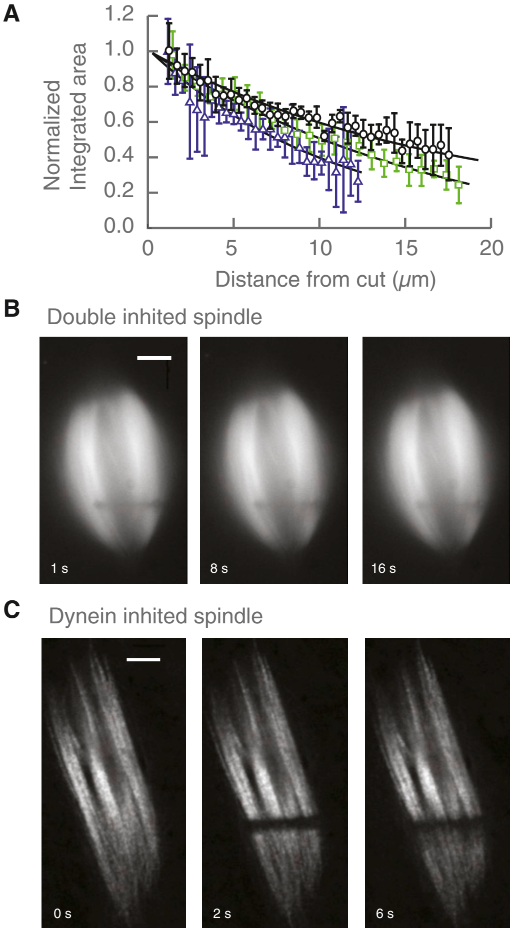

Figure S5. Cuts on Double-Inhibited Spindles and Dynein-Inhibited Spindles, Related to Figure 6

(A) Total normalized rate of intensity loss as a function of the distance from the cut and corresponding exponential fits, for cuts performed on double-inhibited spindles at an average of 7.8 ± 1.6 μm (blue triangles), 20.6 ± 2.0 μm (green squares), and 40.1 ± 1.6 μm (black circles) from the pole toward which the front propagates. The bars are SD.

(B) Series of images of a cut in a double-inhibited spindle for t = 1 s, 8 s, and 16 s. Scale bar, 10 μm.

(C) Series of images of a cut in a dynein-inhibited spindle for t = 0 s, 2 s, and 6 s. Scale bar, 10 μm.